



An Interstellar Synthesis of Glycerol Phosphates

Cheng Zhu^{1,2} , Andrew M. Turner^{1,2}, Matthew J. Abplanalp^{1,2}, Ralf I. Kaiser^{1,2} , Bill Webb³, Gary Siuzdak³ , and Ryan C. Fortenberry⁴ 

¹Department of Chemistry, University of Hawaii at Mānoa, Honolulu, HI 96822, USA; ralfk@hawaii.edu

²W.M. Keck Laboratory in Astrochemistry, University of Hawaii at Mānoa, Honolulu, HI 96822, USA

³Center for Metabolomics and Mass Spectrometry, Scripps Research, La Jolla, CA 92037, USA; siuzdak@scripps.edu

⁴Department of Chemistry & Biochemistry, University of Mississippi, Mississippi 38677, USA

Received 2020 April 17; revised 2020 July 14; accepted 2020 July 15; published 2020 August 5

Abstract

Glycerol phosphates define key molecules pertaining to the Origin of Life question and represent the essential stereo-dictating unit of phospholipids that may self-assemble in aqueous media into prebiotic cell membranes. However, the prebiotic formation pathways to glycerol phosphate have remained elusive to date. In this Letter, we expose a facile pathway toward the abiotic synthesis of glycerol phosphate isomers in phosphine (PH₃) doped interstellar analog ices of methanol (CH₃OH), carbon dioxide (CO₂), or water (H₂O) upon exposure to energetic electrons as a proxy of secondary electrons generated by the penetration of Galactic cosmic rays into interstellar ices at 10 K. The synthetic routes proposed here overcome obstacles of terrestrial-based scenarios that are inhibited by the low solubility of phosphates in water and the unfavorable nature of phosphorylation reactions in aqueous solution, thus revealing a potential pathway to prebiotic glycerol phosphates.

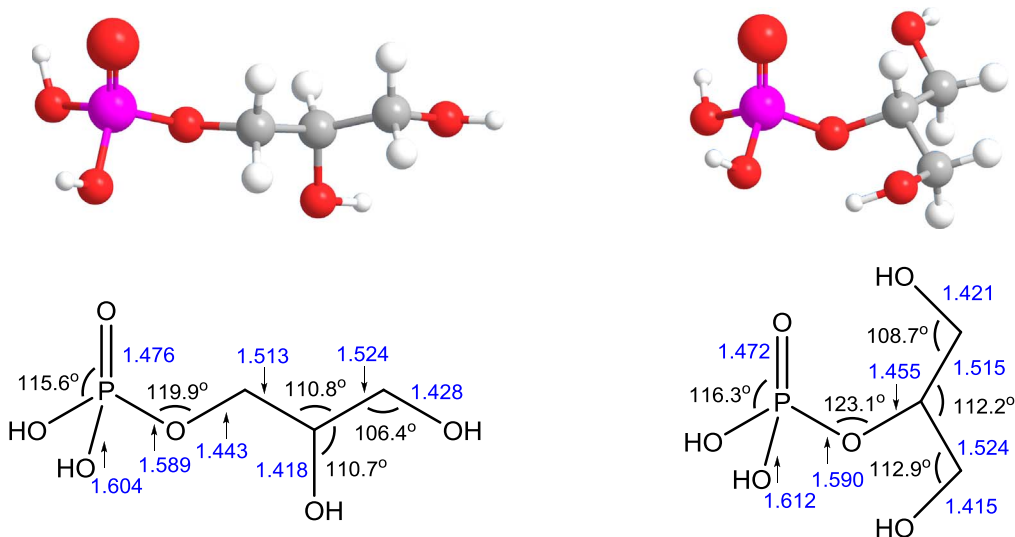
Unified Astronomy Thesaurus concepts: Pre-biotic astrochemistry (2079); Astrochemistry (75); Laboratory astrophysics (2004); Interstellar medium (847); Astrobiology (74)

1. Introduction

For the last decades, the underlying prebiotic pathways directing the synthesis of glycerol phosphates (Scheme 1) and phospholipids on early Earth have remained a topic of vigorous debate (Schwartz 2006; Pasek et al. 2013; Gull et al. 2014; Nam et al. 2017). The phosphate ion (PO₄³⁻) represents a critical molecular backbone in phosphate ester-based biomolecules because it participates in diverse functions like structure formation (phospholipids; Walde 2006), information (RNA/DNA; Fernández-García et al. 2017), and energy storage (ATP/ADP; Fernández-García et al. 2017). However, the limited solubility of terrestrial phosphate minerals such as apatite (Ca₅(PO₄)₃(F,Cl,OH)) in water constrained bioavailable phosphorus for the first organisms on Earth (the “phosphorus problem”; Schwartz 2006; Pasek et al. 2013). Further, the phosphorylation of biomolecules—reactions in which the phosphate group is transferred—is thermodynamically unfavorable in aqueous solution without enzymes (Nam et al. 2017). The Gibbs free energy change ($\Delta_{\text{R}}G$) for an abiotic phosphorylation of, for instance, D-glucose and D-ribose in aqueous solution are at least +14 and +23 kJ mol⁻¹, respectively (the “thermodynamic problem”; Lodish et al. 2000). The susceptibility of organic phosphates to hydrolysis also represents a fundamental challenge (the “water problem”; Nam et al. 2017). Remarkable mechanisms have been proposed to initiate the prebiotic phosphorus chemistry (Pasek et al. 2013; Gull et al. 2014; Nam et al. 2017; Gibard et al. 2018). A terrestrial view advocates that abundant aqueous microdroplets in nature might have been a plausible source for synthesizing phosphate esters, as phosphorylation of various sugars may proceed spontaneously in those microdroplets (Nam et al. 2017). Alternatively, iron–nickel phosphide minerals such as schreibersite ((Fe,Ni)₃P)—proposed to have been delivered to Earth during the heavy bombardment period lasting from 4.1 billion to 3.8 billion years ago—may generate phosphites (PO₃³⁻) and phosphate esters of glycerol under hydrothermal conditions (Pasek et al. 2013). However, the experimental conditions required to form phosphorus-bearing

biorelevant molecules with basic pH values of up to 9.5, along with high concentrations of glycerol of up to 1 M, are often incompatible with early Earth environments (Gull et al. 2014). Although diamidophosphate (DAP) has been found to be able to efficiently phosphorylate lipid precursors under aqueous mild pH conditions, plausible pathways toward the formation of DAP remain undiscovered (Gibard et al. 2018). Therefore, the essential question in prebiotic chemistry, “How was phosphorus introduced into the early Earth?”, has not been conclusively solved.

In this Letter, a facile pathway toward an abiotic synthesis of glycerol phosphates—key constituents of contemporary cell membranes—in interstellar ice analog samples containing phosphine (PH₃), methanol (CH₃OH), and carbon dioxide (CO₂) or water (H₂O) exposed to ionizing radiation in the form of energetic electrons at temperatures of 10 K is revealed (Appendix, Tables A1–A2). Phosphine has been observed in extraterrestrial environments such as in the circumstellar envelope of the carbon star IRC +10216 (Agúndez et al. 2014) and might be formed on interstellar grains via successive hydrogenation of atomic phosphorus (Jiménez-Serra et al. 2018); within our solar system, phosphine was detected in the atmospheres of Jupiter and Saturn (Ridgway et al. 1976; Larson et al. 1980) and is linked to the source of the phosphorus signal in comet 67P/Churyumov–Gerasimenko (Altwegg et al. 2016). Our experiments simulate the processing of phosphine containing interstellar ice by Galactic cosmic ray–induced secondary electrons over typical lifetimes of cold molecular clouds up to a few 10⁷ yr. The abiotic synthesis of glycerol phosphates in interstellar ices bypasses the potential aforementioned “phosphorus,” “thermodynamic,” and “water” obstacles of terrestrial-based scenarios. These problems are overcome by exploiting readily available phosphine as a phosphorus source, by initiating a nonequilibrium chemistry using high energy radiation that supplies a much-needed external energy source, and by taking advantage of water-dominated interstellar ices, thus eliminating the hydrolysis of newly formed glycerol phosphate.



Scheme 1. Molecular structures of glycerol 1/3-phosphate (left, 0 kJ mol^{-1}) and glycerol 2-phosphate (right, 4.7 kJ mol^{-1}). Distances are given in angstrom. The atoms are color coded in light gray (hydrogen), gray (carbon), red (oxygen), and magenta (phosphorous).

2. Experimental Procedures

Our methodology is based on conducting laboratory simulation experiments by exposing low-temperature, astrophysically relevant ices to energetic electrons mimicking secondary electrons generated by the passage of cosmic rays through interstellar ices. The experiments were conducted in an ultrahigh-vacuum (UHV) vessel at base pressures of 1×10^{-10} Torr. Within the chamber, a polished silver wafer was attached to a cold head and cooled down to $10.0 \pm 0.3 \text{ K}$. A gas mixture of phosphine (PH_3), methanol (CH_3OH), and carbon dioxide (CO_2) or water (H_2O) was deposited onto the wafer to form an ice with a composition ratio of PH_3 ($(1.8 \pm 0.4) \times 10^{17} \text{ molecules cm}^{-2}$) : CH_3OH ($(2.7 \pm 0.5) \times 10^{17} \text{ molecules cm}^{-2}$) : CO_2 ($(1.0 \pm 0.2) \times 10^{18} \text{ molecules cm}^{-2}$) = 1.0 : (1.5 ± 0.4) : (5.9 ± 1.7) or PH_3 ($(1.9 \pm 0.4) \times 10^{17} \text{ molecules cm}^{-2}$) : CH_3OH ($(1.9 \pm 0.4) \times 10^{17} \text{ molecules cm}^{-2}$) : H_2O ($(2.1 \pm 0.4) \times 10^{18} \text{ molecules cm}^{-2}$) = 1.0 : (1.0 ± 0.3) : (11.1 ± 3.1) , which is calibrated using quadrupole mass spectrometry (QMS). The ice thickness was determined to be $930 \pm 70 \text{ nm}$ via laser interferometry. Then the ice was irradiated isothermally at $10.0 \pm 0.3 \text{ K}$ with 5 keV electrons for one hour at nominal beam currents of 0 nA (blank), 1000 nA (low dose), and 5000 nA (high dose); (Table A1). Using Monte Carlo simulations (Drouin et al. 2007), the irradiation doses were calculated to be $0.9 \pm 0.1 \text{ eV amu}^{-1}$ for the $\text{PH}_3\text{-CH}_3\text{OH-CO}_2$ ice and $0.8 \pm 0.1 \text{ eV amu}^{-1}$ for the $\text{PH}_3\text{-CH}_3\text{OH-H}_2\text{O}$ ice in the 1000 nA irradiation experiments and were linear to the irradiation current (Table A2). After the irradiation, the ices were annealed to 300 K at a rate of 1 K min^{-1} (temperature programmed desorption (TPD)) to sublime volatile molecules. The chemical modifications of the ices and the development of functional groups were probed on line and in situ via Fourier transform infrared spectroscopy (FTIR). Solid residues remaining at room temperature were dissolved in methanol and analyzed for individual glycerol phosphate isomers exploiting high-performance liquid chromatography coupled with triple quadrupole mass spectrometry (HPLC-QqQ-MS; Appendix).

It is important to link the experiments to the actual conditions in space. Interstellar dust grains at low temperatures (10 K to 20 K) are generally covered with ice mantles a few hundred of nanometers to micrometers in size. The ices are mainly composed of H_2O with significant amounts of, e.g.,

CH_3OH (2% to 15% relative to H_2O ; Bottinelli et al. 2010) and CO_2 (up to 40% relative to H_2O ; Pontoppidan et al. 2008). Phosphine was recently detected in the circumstellar envelope of IRC +10216 with an abundance of $\sim 10^{-8}$ relative to H_2 (Agúndez et al. 2014), which is about 10% relative to H_2O (Cherchneff 2011). The composition ratios of our experimental ices are close to that of the interstellar ices. The irradiation doses inside ice mantles in typical molecular clouds were calculated to be 0.2 eV amu^{-1} to 2 eV amu^{-1} over a time on the order of 10^7 yr (Yeghikyan 2011; Yeghikyan & Barsamyan 2013). Therefore, our irradiation doses correspond to the typical lifetime of molecular clouds of a few 10^7 yr . Note that desorption caused by cosmic rays may alter the ices over the 10^7 yr period.

3. Results and Discussion

3.1. Infrared Spectroscopy

Infrared spectroscopy of irradiated ices represents an exceptional tool to characterize small molecules and functional groups of phosphorus-bearing molecules (Turner et al. 2018). The water-rich ices in our experiments are suitable analog ices, as water represents a major constituent of interstellar ices (Dartois et al. 1999). Nevertheless, as a strong infrared absorber, water along with methanol may conceal several newly emerging infrared absorptions (Figure 1, Tables A3–A8, and Figures A1–A2). Absorptions from alcohol groups [$\nu(\text{HC-OH}/\text{H}_2\text{C-OH})$; ($\sim 3510 \text{ cm}^{-1}$)] and CH/CH_2 groups [$\nu(\text{CH})$; ($3000\text{--}2950 \text{ cm}^{-1}$), $\delta(\text{CH}_n)$; ($1470\text{--}1420 \text{ cm}^{-1}$, $1320\text{--}1260 \text{ cm}^{-1}$)] could be associated with the glycerol building block. Functional groups like the phosphoric hydroxyl [$\nu(\text{P-O-H})$; ($\sim 2700 \text{ cm}^{-1}$, $\sim 2200 \text{ cm}^{-1}$)] and $\text{O}=\text{P-OH}$ groups [$\delta(\text{O}=\text{P-OH})$; ($1600\text{--}1740 \text{ cm}^{-1}$)], as well as the $\text{P}=\text{O}$ group [$\nu(\text{P}=\text{O})$; ($\sim 1200 \text{ cm}^{-1}$)] could be linked to phosphoric acid moieties. Most important, the ester group P-O-C , which is critical in linking glycerol and phosphoric acid to glycerol phosphates, could be detected via two fundamentals [$\nu_{\text{as}}(\text{P-O-C})$; (1000 cm^{-1}), $\nu(\text{C-O})$; (1100 cm^{-1})] even at 10 K (Socrates 2004). These assignments are basically consistent with the computed (Figure A8) and measured IR spectra of glycerol phosphates (Table A4 and Figure A1), e.g., strong absorptions in the range of

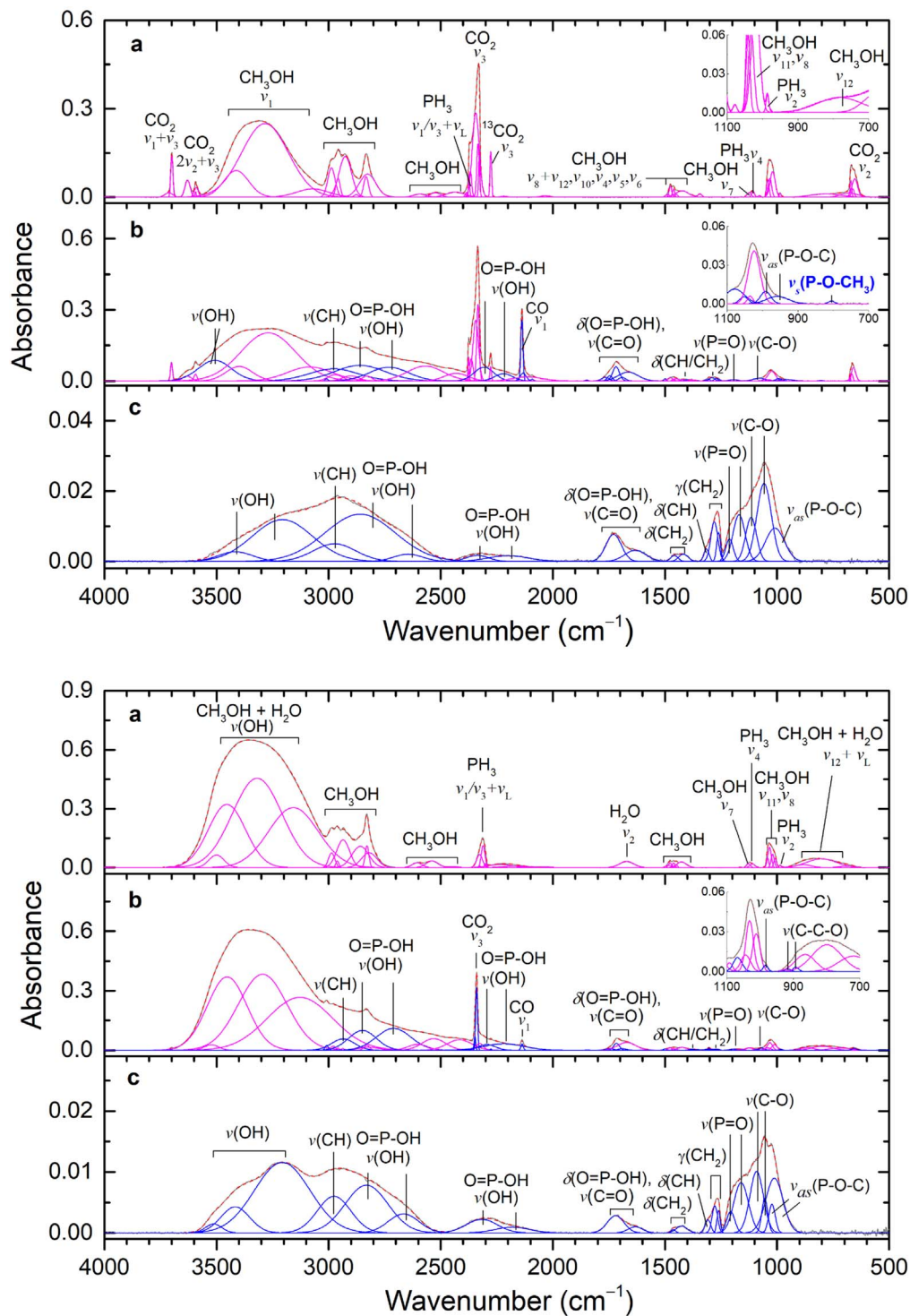


Figure 1. Deconvoluted infrared spectra of phosphine + methanol + carbon dioxide (top) and phosphine + methanol + water ices (bottom). (a) Pristine ices at 10 K. (b) After the high dose irradiation. (c) Residue at 300 K. For clarity, only significant peaks are labeled; detailed assignments are compiled in Tables A3–A8.

3600–3000 cm^{-1} ($\nu(\text{O-H})$), 3000–2850 cm^{-1} ($\nu(\text{C-H})$), 1400–1200 cm^{-1} ($\delta(\text{CH}_n)$), and 1100–1000 cm^{-1} ($\nu(\text{P-O-C})$ and ($\nu(\text{C-O})$). Note that IR spectra may be affected by ice conditions. After the sublimation of the reactants and volatile reaction products during the TPD phase, the aforementioned fundamentals associated with the moieties of glycerol and phosphoric acid are still present in the residues, albeit with lower intensities. Glycerol phosphates hold high melting points (Wishart et al. 2018) and, similar to phosphoric acid (Turner et al. 2018), remain in the

residue. These assignments were confirmed by conducting experiments with ^{18}O - and ^{13}C -labeled ice precursors (Tables A9–A14 and Figures A3–A4), which induced red shifts for the oxygen and carbon containing functional groups, respectively. Most important, the absorptions of the ester group (P–O–C) increase as the radiation dose rises, which provides compelling evidence that this linkage is formed at 10 K as a result of the radiation exposure (Figure A5). Therefore, infrared spectroscopy reveals the existence of key functional groups

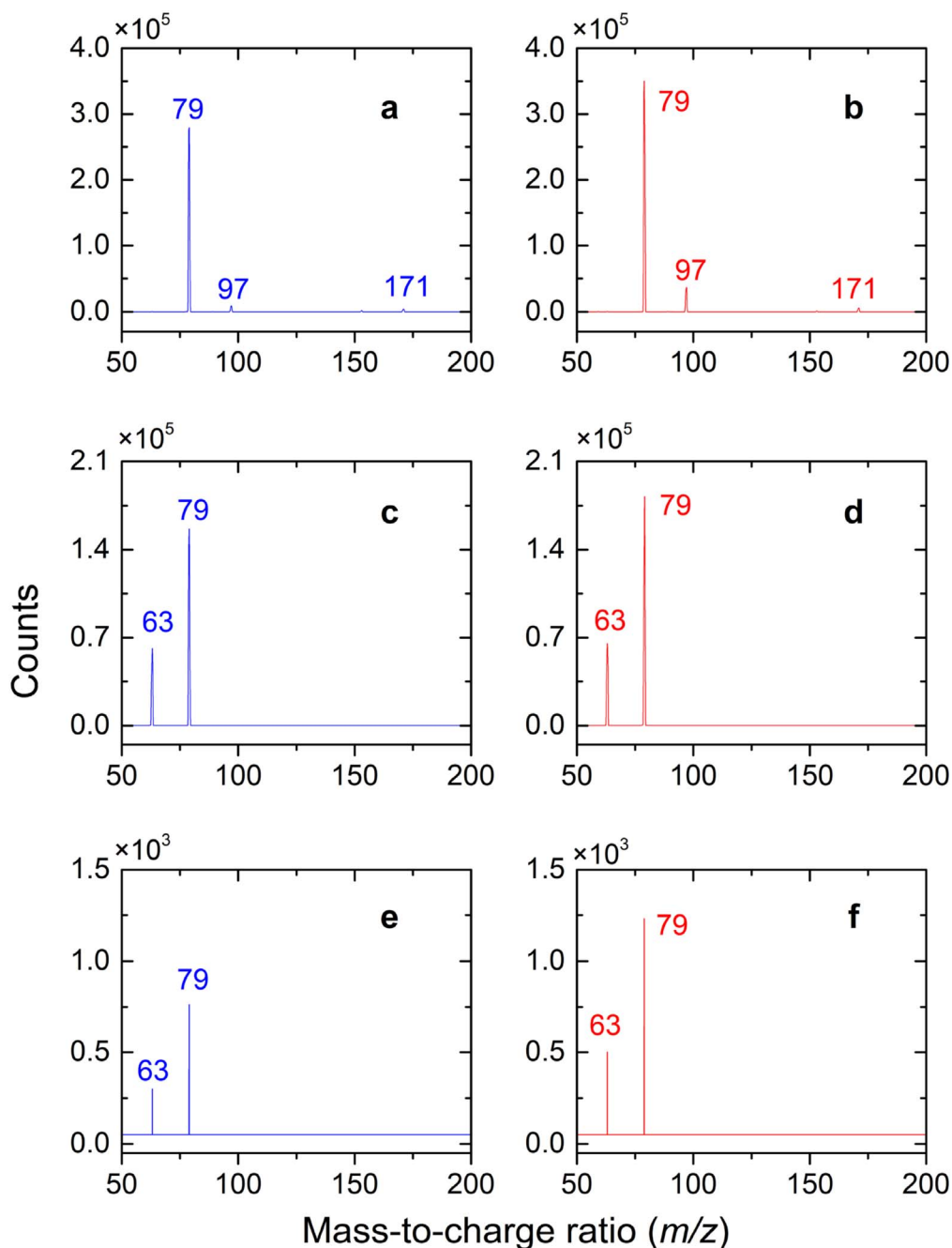


Figure 2. Tandem mass spectral data recorded using a HPLC-QqQ-MS analysis. (a) Standard glycerol 2-phosphate, 20 eV collision energies. (b) Standard glycerol 3-phosphate, 20 eV collision energies. (c) Standard glycerol 2-phosphate, 40 eV collision energies. (d) Standard glycerol 3-phosphate, 40 eV collision energies. (e) Glycerol 2-phosphate in the residue of high dose irradiated phosphine + methanol + water ice, 40 eV collision energies. (f) Glycerol 3-phosphate in the residue of high dose irradiated phosphine + methanol + water ice, 40 eV collision energies. The two isomers have similar tandem mass spectral profiles, but are differentiated based on HPLC retention times.

present in glycerol phosphates formed from the exposure of ices to ionizing radiation at 10 K. However, since the infrared absorptions of individual glycerol phosphates fall in a similar range and, hence, overlap, infrared spectroscopy alone does not allow an identification of discrete glycerol phosphate molecules.

3.2. HPLC-QqQ-MS

To probe individual isomers of glycerol phosphates within the solid residues, these residues were solvated and analyzed utilizing high-performance liquid chromatography (HPLC) coupled with an electrospray ionization (ESI) triple quadrupole mass

spectrometry (QqQ-MS) (Figures 2 and 3 and Figures A6–A7). To maximize the sensitivity, the triple quadrupole mass spectrometer was utilized for multiple reaction mode (MRM) analysis of precursor and corresponding fragment ions, in which the first quadrupole acts as mass filter to select for a specific precursor ion, the second acts as collision cell to induce fragmentation of the precursor ion by collision with inert gas, and the third monitors the precursor specific fragment ions. The ions selection is based on calibration experiments with standards of glycerol 1-/3-phosphate and glycerol 2-phosphate (Appendix). In detail, the first quadrupole mass filter (Q_1) selects the negative precursor ions

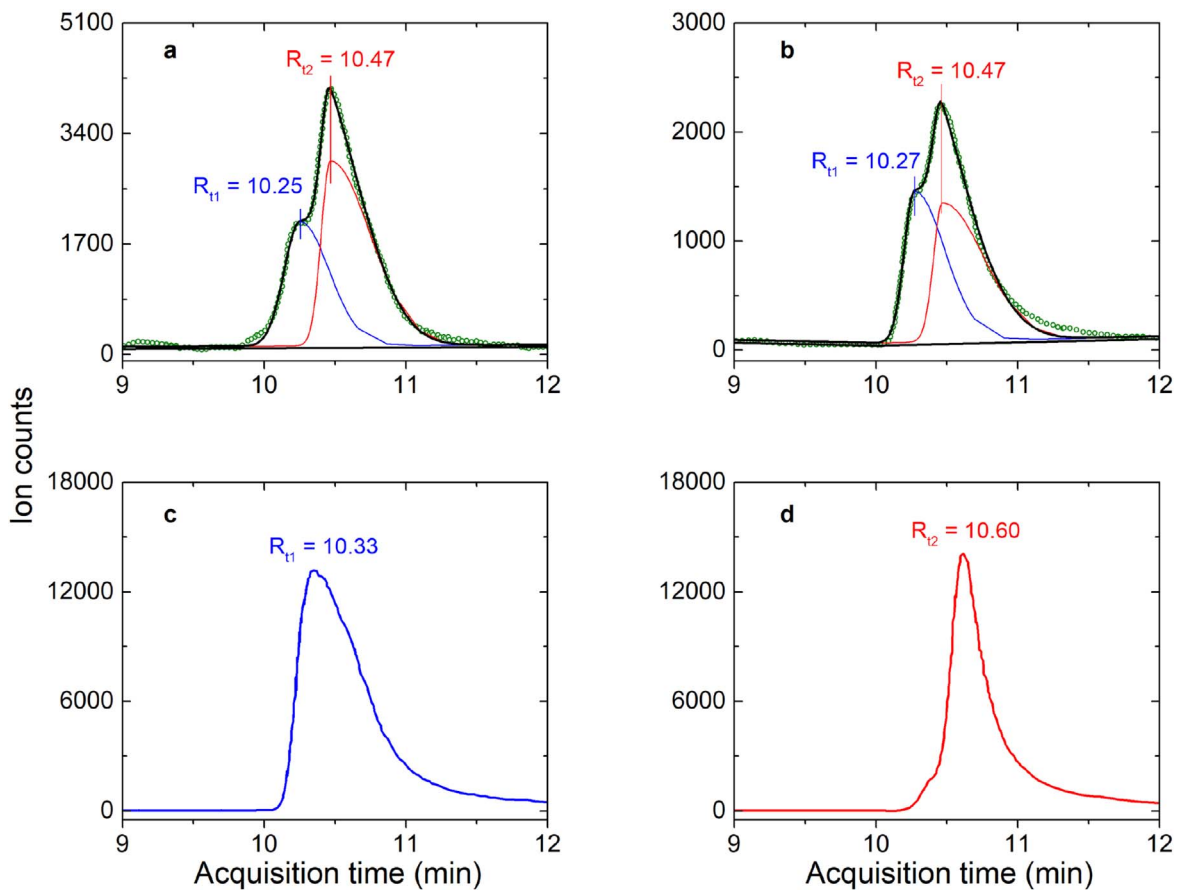


Figure 3. Chromatograms of the $m/z = 79$ fragment ions from $m/z = 171$ exploiting HPLC-QqQ-MS detection. (a) Residue of high dose irradiated phosphine + methanol + water ice. (b) Calibration mixture of glycerol 2-phosphate (0.5 ng) and glycerol 1-/3-phosphate (0.5 ng). (c) Calibration sample of glycerol 2-phosphate (10 ng). (d) Calibration sample of glycerol 1-/3-phosphate (10 ng). Deconvolution of peaks using the bimodal Gaussian mixture model is overlaid in panels (a) and (b). The green lines correspond to experimentally collected data, the blue and red lines outline the deconvoluted fittings; the black lines correspond to the sum of the deconvoluted fittings. Color pattern of the molecular structures: carbon gray, hydrogen cyan, oxygen red, and phosphorous purple.

at mass-to-charge $m/z = 171$ ($C_3H_8O_6P^-$) from the ionized molecules in the solvated residues. These ions collide with the inert gas in the collision chamber (Q_2) and generate fragments; the final quadrupole filter (Q_3) detects these main fragments. Figure 1 shows the counts of the Q_3 detected ions, which include the precursor ions ($m/z = 171$) and fragments from the collisions of the precursor ions with nitrogen in Q_2 at collision energies of 20 eV and 80 eV. Collision at higher energy (80 eV) was selected, as it dissociated all parent ions and generated two prominent fragments at $m/z = 79$ and $m/z = 63$. The newly formed glycerol 1/3- and 2-phosphate isomers were identified explicitly through a comparison of the retention times along with the detection of both major fragments of the negative precursor ion at $m/z = 171$ ($C_3H_8O_6P^-$), which originated from proton loss of the glycerol phosphate isomers ($C_3H_9O_6P$); these fragment ions are $m/z = 79$ (PO_3^-); (quantifier) and $m/z = 63$ (PO_2^-); (qualifier). The quantifier anion is exploited to quantify the glycerol phosphate formed; the qualifier represents a second, independent confirmation of the glycerol phosphate. As shown in Figures 3(a) and A6, two major peaks at retention times of $R_{11} = 10.25$ min and $R_{12} = 10.47$ min were detected for both fragments at $m/z = 79$ and 63. These retention times are in excellent agreement with retention times of both standards for glycerol 2-phosphate and glycerol 1/3-phosphate in mixed conditions at 10.27 min and 10.47 min, respectively. By deconvoluting the overlapping peaks of the quantifier ($m/z = 171 \rightarrow m/z = 79$) using the bimodal

Gaussian mixture model (Yu & Peng 2010) and exploiting the calibration equations (Figure A7), the quantities of the synthesized glycerol 1/3- and 2-phosphates were determined to be 2.6 ± 0.3 ng and 1.9 ± 0.2 ng, resulting in a molar ratio of $(1.4 \pm 0.2) : 1$ and an enhanced formation of the thermodynamically more stable glycerol 1/3-phosphate isomer (Figure A8). The detected glycerol phosphates are not due to contamination during the processing of the silver wafers, because they were not detected in the extractions of a wafer from a blank experiment. Furthermore, the $(1.4 \pm 0.2) : 1$ ratio indicates that the two isomers are not formed after removing the samples from the vacuum systems, as thermodynamic equilibrium calculations predict a branching ratio range of 10.6 to 4.1 at room temperature (Appendix). The conversion yields of phosphine to glycerol 1/3- and 2-phosphates were determined to be $(2.2 \pm 0.4) \times 10^{-3}\%$ and $(1.6 \pm 0.3) \times 10^{-3}\%$, respectively (Appendix), which fall in the same formation efficiency range of prebiotic species such as deoxyribose and nucleobases in interstellar synthesis (Nuevo et al. 2018).

3.3. Proposed Formation Mechanisms

Having confirmed the synthesis of both glycerol 1/3- and 2-phosphate isomers, we now discuss possible formation pathways. Since these products were generated in the solid phase (ice), primary and secondary reactions might be coupled. It is not feasible to determine the contribution of each proposed

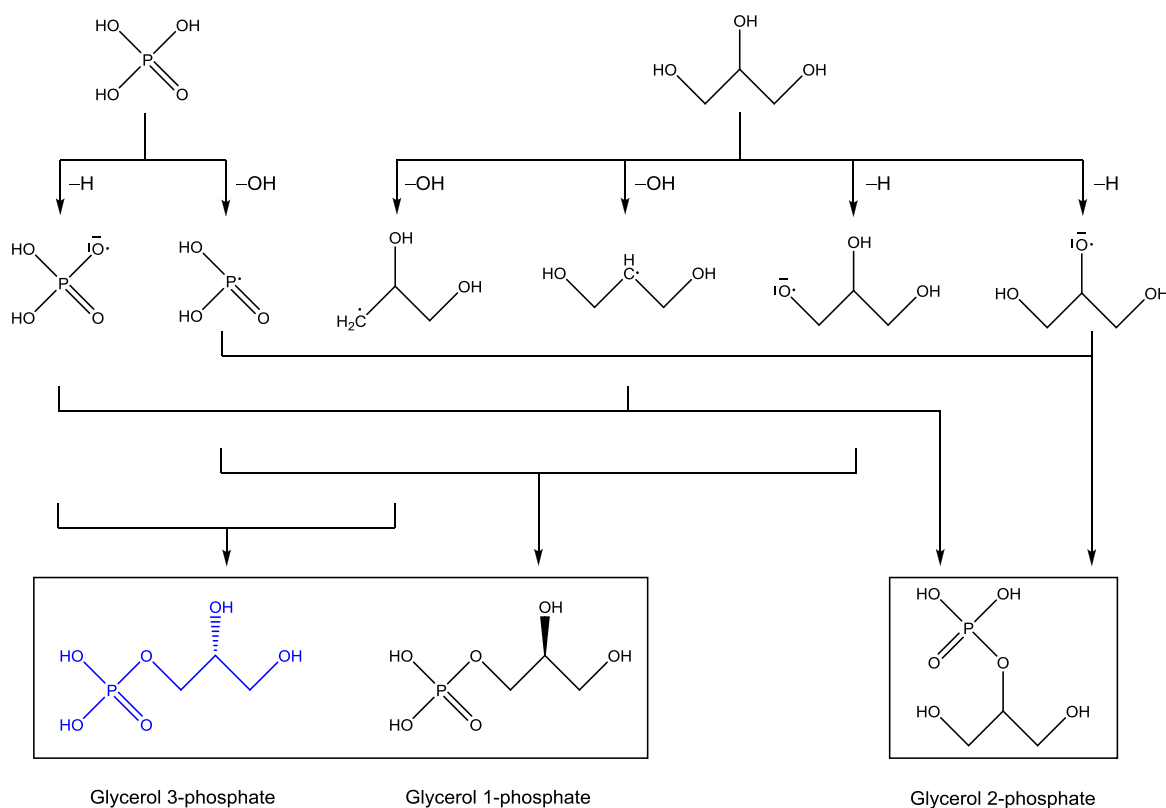


Figure 4. Schematic representation of the formation of glycerol 1/3- and 2-phosphates from phosphoric acid and glycerol.

elementary reaction as in gas phase experiments under single collision conditions (Balucani 2009). Extracting kinetic rate constants linked to the formation of glycerol 1/3- and 2-phosphates based on temporal evolution of FTIR spectra is also not viable because FTIR is unable to identify individual isomers due to the overlapping of their absorption features. However, phosphoric acid (H_3PO_4 ; Turner et al. 2018) and glycerol ($\text{HOCH}_2\text{CH}(\text{OH})\text{CH}_2\text{OH}$; Kaiser et al. 2015)—the key building blocks of glycerol phosphates—were identified previously in energetic electron processed phosphine–water/carbon dioxide and in pure methanol ices, respectively. The interaction of acids and alcohols with ionizing radiation can lead to the loss of atomic hydrogen from the hydroxyl group even at 10 K (Zhu et al. 2019); alternatively, a hydroxyl group can be eliminated. Accounting for the chemically nonequivalent 1/3 versus 2 positions of the hydroxyl groups of glycerol, these processes can yield six distinct radicals (Figure 4). At 10 K, these radicals can recombine if they hold a favorable recombination geometry to yield the infrared spectroscopically observed P–O–C group and hence distinct isomers of glycerol phosphate. These radical mediated molecular mass growth processes have been also considered in the formation of dipeptides from their amino acid monomers (Kaiser et al. 2013).

4. Astrophysical Implications and Conclusions

The present study provides the very first compelling evidence of a facile formation of two phosphoric esters of glycerol—glycerol 1/3-phosphate and glycerol 2-phosphate—upon exposing phosphine doped interstellar analog ices to ionizing radiation mimicking molecular clouds with lifetimes of up to 10^7 yr. These phosphoric esters can be generated abiotically within icy

mantles condensed on interstellar grains in molecular clouds at temperatures as low as 10 K, as evident from the emerging P–O–C group via radical mediated molecular mass growth processes leading to a preferential formation of thermodynamically more stable ($-4.7 \pm 1.2 \text{ kJ mol}^{-1}$) glycerol 1/3-phosphate compared to the glycerol 2-phosphate isomer. Theoretical calculations predict branching ratio ranges of 6.6×10^{30} to 1.9×10^{18} (10 K) and 58 to 11 (175 K), which are distinct from our experimental findings of 1.4 ± 0.2 , exposing a significant overproduction of glycerol 2-phosphate and thus underlining the nonequilibrium nature of the cosmic ray mediated reaction conditions. This work represents a first step toward a systematic elucidation of organophosphorus-bearing molecules in deep space, with glycerol phosphates representing the most complex phosphorus-carrying organics of astrobiological relevance detected in low-temperature simulation experiments thus far. The identification of glycerol phosphates in our ices would suggest that glycerol phosphates could have been incorporated into our solar system from interstellar matter via circumstellar disks (Weidenschilling 2000) and delivered to early Earth by comets or meteorites such as Murchison (Pasek et al. 2013). Although glycerol phosphates have not yet been identified in meteorites (Cooper et al. 1992), the molecular building blocks glycerol ($\text{HOCH}_2\text{CH}(\text{OH})\text{CH}_2\text{OH}$) and phosphate (PO_4^{3-}) were detected in Murchison (Cooper et al. 1992) and also synthesized in analog ices exposed to ionizing radiation (Kaiser et al. 2015; Turner et al. 2018). The extraction of Murchison was prepared with hydrochloric acid, which likely hydrolyzed glycerol phosphates (Bunton & Farber 1969) to glycerol and phosphoric acid.

We speculate that similar phosphoric esters such as ribose-phosphate and deoxyribose-phosphate, the backbones of

genetic materials RNA and DNA, may also be synthesized in deep space in low-temperature ices. Furthermore, previous investigations reported the identification of carboxylic acids up to $C_9H_{19}COOH$ in electron-irradiated ice mixtures of methane (CH_4) and carbon dioxide (CO_2 ; Zhu et al. 2018). Since both the hydrophilic “head”—glycerol 3-phosphate—and hydrophobic “tail”—long chain carboxylic acids—have been synthesized in prebiotic interstellar conditions, it is reasonable to expect the formation of phospholipids to also occur. These phospholipids could self-assemble into stable permeable vesicles storing catalytically active molecules (possibly simple oligopeptides and/or metal ion complexes) and information-carrying molecules, and could provide mild local reaction conditions to generate early cellular life (Bangham 1968). The overall yields of phosphoric esters of up to 4×10^{-3} percent have not pushed the frontiers of HPLC-QqQ-MS to the detection limit, so exciting discoveries leading eventually to glycerides and phospholipids await us. These studies will provide novel concepts and mechanistic pathways for the transformation of low-temperature ices to biorelevant molecules in our universe and hence change how we contemplate the abiotic synthesis of (precursors to) truly complex, phosphorus-carrying biorelevant molecules in deep space.

This work was supported by NASA under Grant NNX16AD27G to The University of Hawaii (R. I. K.) and NNX17AH15G to The University of Mississippi (R. C. F.).

Appendix Irradiation Experiments

The experiments were performed in a stainless steel contamination-free UHV chamber evacuated to a base pressure of 1×10^{-10} Torr, which was rendered using a magnetically suspended turbo molecular pump (Osaka TG420 MCAB) backed by an oil-free scroll pump (Anest Iwata ISP-500). Within the chamber, a polished silver wafer was attached to an oxygen-free, high-conductivity (OFHC) copper target and connected to a two-stage closed-cycle helium refrigerator (CTI-Cryogenics Cryodyne 1020, compressor: CTI-Cryogenics 9600). By utilizing a doubly differentially pumped rotational feedthrough, the substrate is able to be rotated in the horizontal plane. The temperature of the silver wafer was monitored by a silicon diode sensor (Lakeshore DT-470) and regulated in a range of 10 to 300 K with a precision of ± 0.3 K by a programmable temperature controller (Lakeshore 336). After the wafer reached 10.0 ± 0.3 K, a gas mixture of phosphine (PH_3 , Sigma-Aldrich, 99.9995%) and carbon dioxide (CO_2 , Airgas, 99.9999%); (Tables A1 and A2), premixed in a separate chamber, and methanol (CH_3OH , Sigma-Aldrich, HPLC grade) vapor were co-deposited onto it via two glass capillary arrays to form a $PH_3 + CH_3OH + CO_2$ ice. Isotopically labeled $C^{18}O_2$ (95 atom% ^{18}O ; Sigma-Aldrich) and $CH_3^{18}OH$ (95 atom% ^{18}O ; Sigma-Aldrich) or $^{13}CO_2$ (99 atom% ^{13}C ; Sigma-Aldrich) and $^{13}CH_3OH$ (99 atom% ^{13}C ; Sigma-Aldrich) were utilized in duplicate experiments to observe infrared absorption shifts of products. Water (H_2O)-rich ices, $PH_3 + CH_3OH + H_2O$, were prepared by separate deposition of PH_3 and a vapor mixture of CH_3OH and H_2O (Sigma-Aldrich, HPLC grade). The overall thickness of the ice was determined using laser interferometry with one helium-neon laser (CVI Melles Griot; 25-LHP-230) operating at 632.8 nm. The laser light was reflected at an angle of 2° relative to the ice surface normal. Considering the refractive indexes of pure ices $n_{PH_3} = 1.51 \pm 0.04$ (Turner et al. 2015),

Table A1
List of Experiments

#	Precursors	Irradiation current (nA)
1	$PH_3 + CH_3OH + CO_2$	0 (blank)
2	$PH_3 + CH_3OH + H_2O$	0 (blank)
3	$PH_3 + CH_3OH + CO_2$	5000
4	$PH_3 + CH_3OH + CO_2$	1000
5	$PH_3 + CH_3OH + H_2O$	5000
6	$PH_3 + CH_3OH + H_2O$	1000
7	$PH_3 + CH_3^{18}OH + C^{18}O_2$	5000
8	$PH_3 + ^{13}CH_3OH + ^{13}CO_2$	5000

$n_{CH_3OH} = 1.33 \pm 0.04$ (Luna et al. 2018; Hudson et al. 2020), and $n_{CO_2} = 1.27 \pm 0.02$ (Satorre et al. 2008; Loeffler et al. 2016), the ice thickness was calculated to be 930 ± 70 nm. The same thickness was determined for the $PH_3 + CH_3OH + H_2O$ ices ($n_{H_2O} = 1.27 \pm 0.02$) (Dohnalek et al. 2003). To determine the ice composition, we prepared separate pure ices and ice mixtures, determined the ice thickness via laser interferometry, warmed up the ices, and monitored the sublimed molecules using a Balzer QMG 422 quadrupole mass spectrometer (QMS). The column density of the species in pure ice can be determined based on the thickness and density of the ice. With this, the column density of each species in ice mixture can be easily calculated by comparing its QMS signal with that in the pure ice experiment. Based on this protocol, the ice compositions were estimated to be PH_3 ($(1.8 \pm 0.4) \times 10^{17}$ molecules cm^{-2}) : CH_3OH ($(2.7 \pm 0.5) \times 10^{17}$ molecules cm^{-2}) : CO_2 ($(1.0 \pm 0.2) \times 10^{18}$ molecules cm^{-2}) = 1.0 : (1.5 ± 0.4) : (5.9 ± 1.7) , and PH_3 ($(1.9 \pm 0.4) \times 10^{17}$ molecules cm^{-2}) : CH_3OH ($(1.9 \pm 0.4) \times 10^{17}$ molecules cm^{-2}) : H_2O ($(2.1 \pm 0.4) \times 10^{18}$ molecules cm^{-2}) = 1.0 : (1.0 ± 0.3) : (11.1 ± 3.1) .

Mid-infrared (6000 to 400 cm^{-1}) spectra of the ices were recorded utilizing a Nicolet 6700 Fourier transform infrared (FTIR) spectrometer with 4 cm^{-1} spectral resolution. The ices were then isothermally irradiated at 10.0 ± 0.3 K with 5 keV electrons (Specs EQ 22–35 electron source) at a 15° angle to the ice surface normal for one hour at nominal beam currents of 0 nA (blank), 1000 nA (low dose), and 5000 nA (high dose); (Table A1). The extraction efficiency of the electrons is 78.5%. The 5 keV electrons used in the present experiments mimic secondary electrons released during the penetration of Galactic cosmic rays (GCRs) into interstellar ices. GCRs consists primarily of protons (H^+) and helium nuclei (He^{2+}), which have energies predominantly in the range of 10–100 MeV. As a high energy particle penetrates an interstellar ice, the high energy particle loses its energy nearly exclusively (99.999%) via electronic interaction to the target molecules, resulting in bond ruptures and ionization of the molecules (Boyer et al. 2016). These ionization processes release secondary electrons, which lead to further bond rupture and subsequent chemical processes. Therefore, in our experiments, we simulate the effects of GCRs by exploiting energetic electrons as a proxy (Turner et al. 2018; Arumainayagam et al. 2019). Using Monte Carlo simulations (CASINO 2.42; Drouin et al. 2007), the average penetration depths of the electrons were calculated to be 440 ± 50 nm ($PH_3 + CH_3OH + CO_2$) and 480 ± 50 nm ($PH_3 + CH_3OH + H_2O$), which are less than the 930 ± 70 nm ice thickness, ensuring no interaction between the impinging electrons and the silver substrate. After the irradiation, the ices were kept at 10 ± 0.3 K for 1 hr and then heated to 300 K at a

Table A2
Data Applied to Calculate the Average Irradiation Dose per Molecule

Initial Kinetic Energy of the Electrons, E_{init} (keV)	5			
Ice	$\text{PH}_3 + \text{CH}_3\text{OH} + \text{CO}_2$		$\text{PH}_3 + \text{CH}_3\text{OH} + \text{H}_2\text{O}$	
Irradiation current, I (nA)	1000 ± 50	5000 ± 250	1000 ± 50	5000 ± 250
Total number of electrons	$(1.8 \pm 0.2) \times 10^{16}$	$(8.8 \pm 0.9) \times 10^{16}$	$(1.8 \pm 0.2) \times 10^{16}$	$(8.8 \pm 0.9) \times 10^{16}$
Average penetration depth, l (nm) ^a	440 ± 50	440 ± 50	480 ± 50	480 ± 50
Average kinetic energy of backscattered electrons, E_{bs} (keV) ^a	2.84 ± 0.30	2.84 ± 0.30	2.80 ± 0.30	2.80 ± 0.30
Fraction of backscattered electrons, f_{bs} ^a	0.09 ± 0.01	0.09 ± 0.01	0.08 ± 0.01	0.08 ± 0.01
Average kinetic energy of transmitted electrons, E_{trans} (keV) ^a	0	0	0	0
Fraction of transmitted electrons, f_{trans} ^a	0	0	0	0
Irradiated area, A (cm ²)	3.2 ± 0.3	3.2 ± 0.3	3.2 ± 0.3	3.2 ± 0.3
Dose (eV molecule ⁻¹)				
	PH ₃	32.0 ± 5.0	160.0 ± 24.7	26.8 ± 4.1
	CH ₃ OH	30.0 ± 4.6	150.3 ± 23.2	25.2 ± 3.9
	CO ₂	41.3 ± 6.4	206.7 ± 31.9	...
	H ₂ O	14.2 ± 2.2
				70.8 ± 10.9

Note.

^a Parameters obtained from CASINO software v2.42.

rate of 1 K min⁻¹ (TPD). During the complete experiments, in situ mid-infrared spectra (6000 to 400 cm⁻¹) of the ices (Tables A3–A14, and Figures A1–A5) were recorded using the FTIR spectrometer with 4 cm⁻¹ spectral resolution every 2 min.

A.1. HPLC-QqQ-MS

Each wafer with solid residue was placed in a glass beaker and submerged in methanol. This was covered, placed in a sonicating water bath, and sonicated for 15 min. The methanol was harvested and evaporated to dryness under a gentle stream of nitrogen (N₂). The sample was then reconstituted in 25 μl CH₃OH : H₂O (50 : 50), centrifuged to pellet any insolubles, then transferred to an auto-sampler vial. The analysis was carried out using an Agilent 1290 high-performance liquid chromatography (HPLC) system coupled to an Agilent 6495 triple quadrupole mass spectrometer (QqQ-MS). Different compounds in the extractions were first separated using a C18 HPLC Column. The mobile phase consists of A = 20 mM ammonium acetate (CH₃COONH₄) and 20 mM ammonium hydroxide (NH₄OH), pH = 9.6 and B = CH₃OH. The gradient condition was initially set at A : B = 90 : 10 and then ramped to 10 : 90 over 20 min. Stop time was set to 22 min, with a 10 min re-equilibration time. Column effluent was then introduced to the electrospray ionization chamber of the QqQ-MS with a jet stream source, operated in negative mode. Jet stream source conditions were set at: gas flow = 13 L min⁻¹, gas temperature = 523 K, nebulizer pressure = 1810 Torr, sheath gas temperature = 623 K, and sheath gas flow = 12 L min⁻¹. Capillary and nozzle voltages were set to 3000 V and 2000 V, respectively. After ionization, precursor ions at mass-to-charge ratio of $m/z = 171$, which could be due to proton loss of the glycerol phosphate isomers ((M-1)⁻), were selected by a quadrupole mass filter (Q₁) and then fragmented to $m/z = 79$ (PO₃⁻); (qualifier) and $m/z = 63$ (PO₂⁻); (qualifier) by colliding with inert gas nitrogen (N₂) in a collision chamber (Q₂). The qualifier is exploited to quantify the formed glycerol phosphate; the qualifier acts for an additional independent confirmation of the glycerol phosphate. The ions exiting from Q₂ were analyzed by the final quadrupole mass analyzer (Q₃). Glycerol 1/3- and 2-phosphates have similar mass spectral profiles, but are differentiated based on

Table A3
Absorption Peaks Observed in Pristine PH₃ + CH₃OH + CO₂ Ice

Wavenumber (cm ⁻¹)	Assignment
5079	CO ₂ ($2\nu_1 + \nu_3$)
4959	CO ₂ ($\nu_1 + 2\nu_2 + \nu_3$)
4405	CH ₃ OH ($\nu_2/\nu_9 + \nu_4/\nu_6/\nu_{10}$)
4282	CH ₃ OH ($\nu_2/\nu_9 + \nu_4$)
4114	CH ₃ OH ?
4025, 3990, 3949	CH ₃ OH ($\nu_2/\nu_9 + \nu_8$)
3858	CH ₃ OH ?
3713, 3699	CO ₂ ($\nu_1 + \nu_3$)
3629	CO ₂ ...CH ₃ OH complex
3594, 3591	CO ₂ ($2\nu_2 + \nu_3$)
3412, 3284, 3071	CH ₃ OH (ν_1)
2987	CH ₃ OH (ν_2)
2958	CH ₃ OH (ν_9)
2926	CH ₃ OH ($\nu_4 + \nu_5/\nu_4 + \nu_{10}/\nu_5 + \nu_{10}/2\nu_4/2\nu_{10}/2\nu_5$)
2876	CH ₃ OH ($\nu_5/2\nu_{10}$)
2833	CH ₃ OH (ν_3)
2826	CH ₃ OH ($2\nu_6$)
2594	CH ₃ OH ($\nu_4 + \nu_{11}/\nu_7 + \nu_4/\nu_6/\nu_{10}$)
2524	CH ₃ OH ($\nu_6 + \nu_{11}$)
2434	CH ₃ OH ($\nu_6 + \nu_8$)
2385, 2373, 2368	PH ₃ ($\nu_1/\nu_3 + \nu_L$)
2344, 2334	CO ₂ (ν_3)
2328	PH ₃ (ν_3)
2277	¹³ CO ₂ (ν_3)
2219	CH ₃ OH ($2\nu_{11}/2\nu_7$)
2035	CH ₃ OH ($2\nu_8$)
1488	CH ₃ OH ($\nu_8 + \nu_{12}$?)
1476	CH ₃ OH (ν_4)
1462	CH ₃ OH (ν_{10})
1449	CH ₃ OH (ν_5)
1423	CH ₃ OH (ν_6)
1381, 1344	CO ₂ ...CH ₃ OH complex
1159, 1124	CH ₃ OH (ν_7)
1108	PH ₃ (ν_4)
1078	CO ₂ ...CH ₃ OH complex
1041	CH ₃ OH (ν_{11})
1032, 1020	CH ₃ OH (ν_8)
986	PH ₃ (ν_2)
782	CH ₃ OH (ν_{12})
678, 671	CO ₂ ...CH ₃ OH complex
662, 654	CO ₂ (ν_2)

Table A4Comparison of New Absorption Peaks Observed in PH₃ + CH₃OH + CO₂ Ice after 1 hr of Irradiation via 5 keV Electrons at Different Currents with Glycerol 1/3-phosphate

Wavenumber (cm ⁻¹)			Assignment
5000 nA	1000 nA	Glycerol 1/3-phosphate	
3507	3512	3487, 3334, 3150	OH stretch
3009, 2977	3006, 2961	2948, 2896	CH, CH ₂ (CH stretch)
2860, 2731, 2568	2729, 2594	2841, 2665	O = P–OH (OH Stretch)
2308	2303	2308	P–H and O = P–OH (OH) stretch
2219	2238	2180	O = P–OH (OH Stretch)
2138, 2132	2139		CO (ν_1)
2092	2092		¹³ CO (ν_1)
1848	1849		HCO (ν_3)
1766, 1745, 1718, 1691	1770, 1746, 1718, 1690	1642	O = P–OH (OH bending) and C = O stretch
1500	1502		H ₂ CO (ν_3)
Overlapped with methanol	Overlapped with methanol	1459, 1424	CH ₂ scissoring
1398, 1352, 1317	1381, 1344	1336	CH wagging coupled with OH bending
1305	1303		CH ₄ (ν_4)
1291, 1271, 1258	1286, 1275, 1272	1253	CH ₂ twisting coupled with OH bending
1195	1192	1195	P = O stretch
1080, 1052	1057	1109, 1051	C–O stretch
991, 958	971	1006, 963	asym. P–O–C stretch
805		832	sym. P–O–C stretch

Table A5Comparison of Absorption Peaks Observed in Residue of PH₃ + CH₃OH + CO₂ Ice after Irradiation at Different Currents with Glycerol 1/3-phosphate

Wavenumber (cm ⁻¹)			Assignment
5000 nA	1000 nA	Glycerol 1/3-phosphate	
3415, 3206	3409, 3219	3487, 3334, 3150	O–H stretch
2973	2974	2948, 2896, 2841	CH, CH ₂ (CH stretch)
2859, 2645, 2336, 2199	2850, 2642, 2343, 2203	2841, 2665, 2308, 2180	O = P–OH (OH Stretch)
1729, 1632	1725	1642	O = P–OH (OH bending) and C = O stretch
1458, 1418	1448	1459, 1424	CH ₂ scissoring
1315		1336	CH twisting coupled with OH bending
1280, 1261	1294, 1268	1253	CH ₂ twisting coupled with OH bending
1212, 1170	1192	1195	P = O stretch
1116, 1058	1103, 1052	1109, 1051	C–O stretch
1009	1008	1006, 963	asym. P–O–C stretch
		832	Weak, sym. P–O–C stretch

HPLC retention time. Two elution peaks with retention times of $R_{t1} = 1.86 \pm 0.02$ and $R_{t2} = 2.05 \pm 0.04$ min were detected in the residues of all four irradiation experiments (experiments 3–6 in Table A1). It is critical to note that none of these peaks appeared in blank experiments. The latter peak at 2.05 ± 0.04 min was assigned to glycerol 1/3-phosphate by comparison with the chromatogram of a standard. The former peak was proposed to be glycerol 2-phosphate, but not confirmed due to the lack of calibration compound. Since glycerol 1/3-phosphate is most abundant in the residue of the high dose irradiated PH₃ + CH₃OH + H₂O ice, after getting glycerol 2-phosphate, we repeated this experiment and analyzed the residue and two standards using a SeQuant ZIC-pHILIC 2.1 × 150 mm column (Figure A6). Calibration experiments using standard glycerol 1/3- and 2-phosphate mixtures with different concentrations were performed. Figure A7 depicts the calibration curves for both isomers. To quantify the detected isomers in the residue of the high dose irradiated phosphine—methanol—water, we deconvoluted the chromatogram of the quantifier ($m/z = 171 \rightarrow m/z = 79$ transition) exploiting the bimodal Gaussian mixture model, which is better at fitting asymmetric LC–MS peaks compared to the

Gaussian mixture model (Yu & Peng 2010). With the peak areas of 1231 ± 130 count · minute and 764 ± 80 count · minute and corresponding calibration equations (Figure A7), the quantities of the synthesized glycerol 1/3- and 2-phosphates were determined to be 2.6 ± 0.3 ng and 1.9 ± 0.2 ng, respectively.

A.2. Conversion Yield

Considering the column densities and the ice area of 3.2 ± 0.3 cm² (Table A2), the total molecule numbers in pristine PH₃ + CH₃OH + H₂O ice were calculated to be $(6.0 \pm 1.3) \times 10^{17}$ molecules for PH₃, $(6.0 \pm 1.3) \times 10^{17}$ molecules for CH₃OH, and $(6.6 \pm 1.5) \times 10^{18}$ molecules for H₂O. Electron irradiation in our experiment does not change the ice thickness, and therefore the optical interference effects (Teolis et al. 2007) on the absorption coefficient of each IR peak are the same for pristine and irradiated ices (Loeffler et al. 2006). By comparing the peak areas of PH₃ (ν_4), CH₃OH (ν_{11} and ν_8), and H₂O (ν_L) before and after the high dose irradiation, the irradiation consumed molecules can be determined to be 690 ± 140 nmol ($(4.1 \pm 0.8) \times 10^{17}$ molecules), 710 ± 150

Table A6Absorption Peaks Observed in Pristine PH₃ + CH₃OH + H₂O Ice

Wavenumber (cm ⁻¹)	Assignment
5141, 5053	H ₂ O ($\nu_2 + \nu_3$)
4919	
4403	CH ₃ OH ($\nu_2/\nu_9 + \nu_4/\nu_6/\nu_{10}$)
4277	CH ₃ OH ($\nu_2/\nu_9 + \nu_4$)
4101	
4000, 3984, 3943	CH ₃ OH ($\nu_2/\nu_9 + \nu_8$)
3856	CH ₃ OH ?
3500, 3453, 3319, 3157	CH ₃ OH+H ₂ O (OH stretch)
2987	CH ₃ OH (ν_2)
2962	CH ₃ OH (ν_9)
2935	CH ₃ OH ($\nu_4 + \nu_5/\nu_4 + \nu_{10}/\nu_5 + \nu_{10}/2\nu_4/2\nu_{10}/2\nu_5$)
2858	CH ₃ OH ($2\nu_5/2\nu_{10}$)
2829	CH ₃ OH (ν_3)
2819	CH ₃ OH ($2\nu_6$)
2605	CH ₃ OH ($\nu_4 + \nu_{11}/\nu_7 + \nu_4/\nu_6/\nu_{10}$)
2538	CH ₃ OH ($\nu_6 + \nu_{11}$)
2443	CH ₃ OH ($\nu_6 + \nu_8$)
2362, 2326, 2311	PH ₃ ($\nu_1/\nu_3 + \nu_L$)
2301	PH ₃ (ν_3)
2235	CH ₃ OH ($2\nu_{11}/2\nu_7$)
2162	PH ₃ ($2\nu_4$)
2034	CH ₃ OH ($2\nu_8$)
1675	H ₂ O (ν_2)
1484	CH ₃ OH ($\nu_8 + \nu_{12}$?)
1477	CH ₃ OH (ν_4)
1461	CH ₃ OH (ν_{10})
1449	CH ₃ OH (ν_5)
1426	CH ₃ OH (ν_6)
1161, 1130	CH ₃ OH (ν_7)
1115	PH ₃ (ν_4)
1045	CH ₃ OH (ν_{11})
1033, 1020	CH ₃ OH (ν_8)
1008	¹³ CH ₃ OH (ν_8)
986	PH ₃ (ν_2)
882, 802, 690	CH ₃ OH (ν_{12}) + H ₂ O (ν_L)

nmol ($(4.3 \pm 0.9) \times 10^{17}$ molecules), and 7000 ± 1500 nmol ($(4.2 \pm 0.9) \times 10^{18}$ molecules), respectively. The HPLC-QqQ-MS analysis detected 0.015 ± 0.002 nmol (2.6 ± 0.3 ng) of glycerol 1/3-phosphate and 0.011 ± 0.001 nmol (1.9 ± 0.2 ng) of glycerol 2-phosphate. Therefore, the conversion yields of glycerol 1/3- and 2-phosphates with respect to the phosphine reactant are $(2.2 \pm 0.4) \times 10^{-3}\%$ and $(1.6 \pm 0.3) \times 10^{-3}\%$ yields, which are equivalent to $(2.1 \pm 0.3) \times 10^{-8}$ and $(1.5 \pm 0.2) \times 10^{-8}$ molecules eV⁻¹ efficiency, respectively.

A.3. Branching Ratio and Formation Conditions

The determination of the branching ratio of glycerol 1/3- and 2-phosphates provides valuable information on the conditions of their synthesis. If these species are formed within a thermodynamical equilibrium process during the TPD, the quotient of their concentrations is connected with an equilibrium constant K :

$$K = [\text{glycerol 1/3 - phosphate}] / [\text{glycerol 2 - phosphate}] = e^{-\Delta_R G / RT} \quad (\text{A1})$$

where T is the temperature, R is the ideal gas constant, and $\Delta_R G$ is the difference between the standard Gibbs free energies of glycerol

Table A7New Absorption Peaks Observed in PH₃ + CH₃OH + H₂O Ice after 1 hr of Irradiation via 5 keV Electrons at Different Currents

Wavenumber (cm ⁻¹)		Assignment
5000 nA	1000 nA	
3700	3698	CO ₂ ($\nu_1 + \nu_3$)
3008, 2935	3002, 2920	CH, CH ₂ (CH stretch)
2848, 2709	2740	O = P-OH (OH Stretch)
2347, 2340	2342, 2340	CO ₂ (ν_3)
2294	2284	P-H and O = P-OH (OH stretch)
2276	2276	¹³ CO ₂ (ν_3)
2219	2207	O = P-OH (OH stretch)
2137	2136	CO (ν_1)
1846	1845	HCO (ν_3)
1746, 1716, 1689	1747, 1718	O = P-OH (OH bending) and C = O stretch
1499	1499	H ₂ CO (ν_3)
1377, 1352, 1340, 1312	1376, 1351, 1332	CH wagging coupled with OH bending
1303	1304	CH ₄ (ν_4)
1282, 1266, 1256, 1218	1279, 1264, 1253	CH ₂ twisting coupled with OH bending
1191	1187	P = O stretch
1067	1056	C-O stretch
983	974	asym. P-O-C stretch
917, 893	915, 893	C-C-O stretch
655	651	CO ₂ (ν_2)

Table A8Absorption Peaks Observed in Residue of PH₃ + CH₃OH + H₂O Ice after Irradiation at Different Currents

Wavenumber (cm ⁻¹)		Assignment
5000 nA	1000 nA	
3513, 3416, 3207	3489, 3405, 3234	O-H stretch
2975	2970	CH, CH ₂ (CH stretch)
2831, 2665, 2317, 2180	2859, 2642, 2305, 2171	O = P-OH (OH stretch)
1720, 1632	1724	O = P-OH (OH bending) and C = O stretch
1463, 1426	1433	CH ₂ scissoring
1309	1303	CH twisting coupled with OH bending
1261	1273	CH ₂ twisting coupled with OH bending
1207, 1161	1188, 1147	P = O stretch
1091, 1055	1086, 1054	C-O stretch
1023, 1012	1021	asym. P-O-C stretch

1/3- and 2-phosphates. As the relative energies of the two isomers are unknown, we performed accurate quantum mechanical calculations. The geometries of the isomers are optimized with B3LYP (Becke 1993) via the aug-cc-pVTZ basis set (Peterson & Dunning 1995) within the Gaussian09 quantum chemistry program (Frisch et al. 2009). Vibrational frequencies are computed at this same level of theory in order to ensure the structures are not maxima. The resulting harmonic zero-point vibrational energies (ZPVEs) are then incorporated into the relative energy computations. Coupled cluster singles, doubles, and perturbative triples [CCSD(T)] single-point energies (Raghavachari et al. 1989) are computed with both the aug-cc-pVDZ and aug-cc-pVTZ basis sets

Table A9Absorption Peaks Observed in Pristine $\text{PH}_3 + \text{CH}_3^{18}\text{OH} + \text{C}^{18}\text{O}_2$ Ice

Wavenumber (cm^{-1})	Assignment
4815	C^{18}O_2 ($2\nu_1 + \nu_3$)
4699	C^{18}O_2 ($\nu_1 + 2\nu_2 + \nu_3$)
4406	$\text{CH}_3^{18}\text{OH}$ ($\nu_2/\nu_9 + \nu_4/\nu_6/\nu_{10}$)
4282	$\text{CH}_3^{18}\text{OH}$ ($\nu_2/\nu_9 + \nu_4$)
3995, 3961, 3915	$\text{CH}_3^{18}\text{OH}$ ($\nu_2/\nu_9 + \nu_8$)
3831	$\text{CH}_3^{18}\text{OH}$?
3621, 3620	C^{18}O_2 ($\nu_1 + \nu_3$)
3603, 3526	$\text{C}^{18}\text{O}_2 \cdots \text{CH}_3^{18}\text{OH}$ complex
3510	C^{18}O_2 ($2\nu_2 + \nu_3$)
3404, 3278, 3074	$\text{CH}_3^{18}\text{OH}$ (ν_1)
2988	$\text{CH}_3^{18}\text{OH}$ (ν_2)
2958	$\text{CH}_3^{18}\text{OH}$ (ν_9)
2922	$\text{CH}_3^{18}\text{OH}$ ($\nu_4 + \nu_5/\nu_4 + \nu_{10}/\nu_5 + \nu_{10}/2\nu_4/2\nu_{10}/2\nu_5$)
2873	$\text{CH}_3^{18}\text{OH}$ ($\nu_5/2\nu_{10}$)
2835	$\text{CH}_3^{18}\text{OH}$ (ν_3)
2809	$\text{CH}_3^{18}\text{OH}$ ($2\nu_6$)
2589	$\text{CH}_3^{18}\text{OH}$ ($\nu_4 + \nu_{11}/\nu_7 + \nu_4/\nu_6/\nu_{10}$)
2521	$\text{CH}_3^{18}\text{OH}$ ($\nu_6 + \nu_{11}$)
2384	$\text{CH}_3^{18}\text{OH}$ ($\nu_6 + \nu_8$)
2313, 2300, 2294	C^{18}O_2 (ν_3) and PH_3 (ν_3)
2259	$^{18}\text{O}^{13}\text{CO}$ (ν_3)
2246, 2241	$^{13}\text{C}^{18}\text{O}_2$ (ν_3)
2226	$\text{CH}_3^{18}\text{OH}$ ($2\nu_{11}/2\nu_7$)
1990	$\text{CH}_3^{18}\text{OH}$ ($2\nu_8$)
1479	$\text{CH}_3^{18}\text{OH}$ ($\nu_8 + \nu_{12}$?)
1475	$\text{CH}_3^{18}\text{OH}$ (ν_4)
1462	$\text{CH}_3^{18}\text{OH}$ (ν_{10})
1449	$\text{CH}_3^{18}\text{OH}$ (ν_5)
1417	$\text{CH}_3^{18}\text{OH}$ (ν_6)
1339	$\text{C}^{18}\text{O}_2 \cdots \text{CH}_3^{18}\text{OH}$ complex
1158, 1122	$\text{CH}_3^{18}\text{OH}$ (ν_7)
1107	PH_3 (ν_4)
1078	$\text{C}^{18}\text{O}_2 \cdots \text{CH}_3^{18}\text{OH}$ complex
1034	$\text{CH}_3^{18}\text{OH}$ (ν_{11})
1012, 1002	$\text{CH}_3^{18}\text{OH}$ (ν_8)
984	PH_3 (ν_2)
832, 715	$\text{CH}_3^{18}\text{OH}$ (ν_{12})
661	$\text{C}^{18}\text{O}_2 \cdots \text{CH}_3^{18}\text{OH}$ complex
652, 632	C^{18}O_2 (ν_2)

from the B3LYP/aug-cc-pVTZ minimum geometries of the two isomers. The CCSD(T) computations are undertaken with the Molpro2015.1 quantum chemistry program (Werner et al. 2015). The CCSD(T)/aug-cc-pVDZ and aug-cc-pVTZ energies are extrapolated to the complete basis set (CBS) limit via a 2-point formula (Huh & Lee 2003) for each isomer. The relative energies are then computed as the difference between the CCSD(T)/CBS energies corrected with the B3LYP/aug-cc-pVTZ ZPVEs. Figure A8 compiles the computed Cartesian coordinates, vibrational frequencies, IR intensities, and relative energies of the two species. The glycerol 1/3-phosphate isomer is found to be more stable than glycerol 2-phosphate by 4.7 kJ mol^{-1} . Hence, within

Table A10New Absorption Peaks Observed in $\text{PH}_3 + \text{CH}_3^{18}\text{OH} + \text{C}^{18}\text{O}_2$ Ice after 1 hr of Irradiation via 5 keV Electrons at 5000 nA

Wavenumber (cm^{-1})	Assignment
3512	^{18}OH stretch
3011, 2910	CH, CH_2 (CH stretch)
2895, 2718, 2557	O = P- ^{18}OH (^{18}OH stretch)
2301	P-H and $^{18}\text{O} = \text{P}-^{18}\text{OH}$ (^{18}OH stretch)
2218	O = P- ^{18}OH (^{18}OH stretch)
2139	CO (ν_1)
2094, 2087	C^{18}O (ν_1)
1804	HC^{18}O (ν_3)
1742, 1705 1685, 1662	$^{18}\text{O} = \text{P}-^{18}\text{OH}$ (^{18}OH bending) and C = ^{18}O stretch
1486	$\text{H}_2\text{C}^{18}\text{O}$ (ν_3)
1383, 1352, 1333	CH wagging coupled with ^{18}OH bending
1304	CH_4 (ν_4)
1279, 1261	CH_2 twisting coupled with ^{18}OH bending
1181	P = ^{18}O stretch
1041	$\text{C}-^{18}\text{O}$ stretch
985, 937	asym. P- ^{18}O -C stretch
795	sym. P- ^{18}O -C stretch

Table A11Absorption Peaks Observed in Residue of $\text{PH}_3 + \text{CH}_3^{18}\text{OH} + \text{C}^{18}\text{O}_2$ Ice after Irradiation at Different Currents

Wavenumber (cm^{-1})	Assignment
3318, 3162	^{18}O -H stretch
2979	CH, CH_2 (CH stretch)
2858, 2635, 2325, 2179	$^{18}\text{O} = \text{P}-^{18}\text{OH}$ (^{18}OH stretch)
1699, 1614	$^{18}\text{O} = \text{P}-^{18}\text{OH}$ (^{18}OH bending) and C = ^{18}O stretch
1462, 1431	CH_2 scissoring (Aliphatic)
1316	CH twisting coupled with ^{18}OH bending
1282, 1264	CH_2 twisting coupled with ^{18}OH bending
1201, 1151	P = ^{18}O stretch
1094, 1027	$\text{C}-^{18}\text{O}$ stretch
990	asym. P- ^{18}O -C stretch

the temperature range from 10 K to 175 K, with the latter representing the highest sublimation temperature of the precursors (H_2O), the branching ratio of glycerol 1/3-phosphate to glycerol 2-phosphate is expected to be in the range of 2.5×10^{24} (10 K) and 25 (175 K) if they are formed under thermal, equilibrium conditions. However, this range is significantly higher than the experimentally derived branching ratio of 1.4 ± 0.2 , exposing an overproduction of glycerol 2-phosphate. Therefore, our results indicate that the two isomers are formed through nonequilibrium processes at ultralow temperatures, but not under thermal equilibrium conditions during the TPD phase. This finding is consistent with the detection of the P-O-C stretching peaks after the irradiation of the ices at 10 K. The detected glycerol phosphates are also not generated after the residues were removed from the

Table A12Absorption Peaks Observed in Pristine $\text{PH}_3 + {}^{13}\text{CH}_3\text{OH} + {}^{13}\text{CO}_2$ Ice

Wavenumber (cm^{-1})	Assignment
4971	${}^{13}\text{CO}_2$ ($2\nu_1 + \nu_3$)
4863	${}^{13}\text{CO}_2$ ($\nu_1 + 2\nu_2 + \nu_3$)
4387	${}^{13}\text{CH}_3\text{OH}$ ($\nu_2/\nu_9 + \nu_4/\nu_6/\nu_{10}$)
4273	${}^{13}\text{CH}_3\text{OH}$ ($\nu_2/\nu_9 + \nu_4$)
4083	?
3995, 3961, 3915	${}^{13}\text{CH}_3\text{OH}$ ($\nu_2/\nu_9 + \nu_8$)
3831	${}^{13}\text{CH}_3\text{OH}$?
3629, 3619	${}^{13}\text{CO}_2$ ($\nu_1 + \nu_3$)
3573, 3531	${}^{13}\text{CO}_2 \cdots {}^{13}\text{CH}_3\text{OH}$ complex
3502	${}^{13}\text{CO}_2$ ($2\nu_2 + \nu_3$)
3413, 3289, 3052	${}^{13}\text{CH}_3\text{OH}$ (ν_1)
2977	${}^{13}\text{CH}_3\text{OH}$ (ν_2)
2951	${}^{13}\text{CH}_3\text{OH}$ (ν_9)
2917	${}^{13}\text{CH}_3\text{OH}$ ($\nu_4 + \nu_5/\nu_4 + \nu_{10}/\nu_5 + \nu_{10}/2\nu_4/2\nu_{10}/2\nu_5$)
2865	${}^{13}\text{CH}_3\text{OH}$ ($\nu_5/2\nu_{10}$)
2829	${}^{13}\text{CH}_3\text{OH}$ (ν_3)
2815	${}^{13}\text{CH}_3\text{OH}$ ($2\nu_6$)
2589, 2578	${}^{13}\text{CH}_3\text{OH}$ ($\nu_4 + \nu_{11}/\nu_7 + \nu_4/\nu_6/\nu_{10}$)
2511	${}^{13}\text{CH}_3\text{OH}$ ($\nu_6 + \nu_{11}$)
2381	${}^{13}\text{CH}_3\text{OH}$ ($\nu_6 + \nu_8$)
2344	CO_2 (ν_3)
2325, 2302	PH_3 (ν_3)
2280, 2266	${}^{13}\text{CO}_2$ (ν_3)
2216	${}^{13}\text{CH}_3\text{OH}$ ($2\nu_{11}/2\nu_7$)
1990	${}^{13}\text{CH}_3\text{OH}$ ($2\nu_8$)
1488	${}^{13}\text{CH}_3\text{OH}$ ($\nu_8 + \nu_{12}$?)
1474	${}^{13}\text{CH}_3\text{OH}$ (ν_4)
1460	${}^{13}\text{CH}_3\text{OH}$ (ν_{10})
1448	${}^{13}\text{CH}_3\text{OH}$ (ν_5)
1415	${}^{13}\text{CH}_3\text{OH}$ (ν_6)
1363, 1339	${}^{13}\text{CO}_2 \cdots {}^{13}\text{CH}_3\text{OH}$ complex
1150, 1122	${}^{13}\text{CH}_3\text{OH}$ (ν_7)
1106	PH_3 (ν_4)
1076	${}^{13}\text{CO}_2 \cdots {}^{13}\text{CH}_3\text{OH}$ complex
1023	${}^{13}\text{CH}_3\text{OH}$ (ν_{11})
1017, 1007	${}^{13}\text{CH}_3\text{OH}$ (ν_8)
986	PH_3 (ν_2)
832, 715	${}^{13}\text{CH}_3\text{OH}$ (ν_{12})
649	${}^{13}\text{CO}_2 \cdots {}^{13}\text{CH}_3\text{OH}$ complex
638	${}^{13}\text{CO}_2$ (ν_2)

Table A13New Absorption Peaks Observed in $\text{PH}_3 + {}^{13}\text{CH}_3\text{OH} + {}^{13}\text{CO}_2$ Ice after 1 hr of Irradiation via 5 keV Electrons at 5000 nA

Wavenumber (cm^{-1})	Assignment
3505	OH stretch
3000	${}^{13}\text{CH}_2$, ${}^{13}\text{CH}$ (${}^{13}\text{CH}$ stretch)
2899, 2731, 2566	O = P-OH (OH stretch)
2328	P-H and O = P-OH (OH stretch)
2253	O = P-OH (OH stretch)
2141	CO (ν_1)
2097, 2090	${}^{13}\text{CO}$ (ν_1)
1809	$\text{H}{}^{13}\text{CO}$ (ν_3)
1722, 1711, 1681, 1651	O = P-OH (OH bending) and ${}^{13}\text{C} = \text{O}$ stretch
1499	H_2 ${}^{13}\text{CO}$ (ν_3)
1342, 1310	${}^{13}\text{CH}$ wagging coupled with OH bending
1297	${}^{13}\text{CH}_4$ (ν_4)
1276, 1259	${}^{13}\text{CH}_2$ twisting coupled with OH bending
1202	P = O stretch
1045	${}^{13}\text{C}-\text{O}$ stretch
990, 951	asym. P-O- ${}^{13}\text{C}$ stretch
779	sym. P-O- ${}^{13}\text{C}$ stretch

Table A14Absorption Peaks Observed in Residue of $\text{PH}_3 + {}^{13}\text{CH}_3\text{OH} + {}^{13}\text{CO}_2$ Ice after Irradiation at 5000 nA

Wavenumber (cm^{-1})	Assignment
3430, 3200	O-H stretch
2926	${}^{13}\text{CH}_2$, ${}^{13}\text{CH}$ (${}^{13}\text{CH}$ stretch)
2779, 2649, 2331, 2205	O = P-OH (OH stretch)
1688, 1604	O = P-OH (OH bending) and ${}^{13}\text{C} = \text{O}$ stretch
1456, 1425	${}^{13}\text{CH}_2$ scissoring
1305	${}^{13}\text{CH}$ twisting coupled with OH bending
1279, 1261	${}^{13}\text{CH}_2$ twisting coupled with OH bending
1213, 1166	P = O stretch
1109, 1049	${}^{13}\text{C}-\text{O}$ stretch
976	asym. P-O- ${}^{13}\text{C}$ stretch

vacuum system, since the ratio of glycerol 1/3-phosphate to glycerol 2-phosphate formed at room temperature should be in a range of 10.6 to 4.1, which is considerably higher than the detected value of $(1.4 \pm 0.2) : 1$.

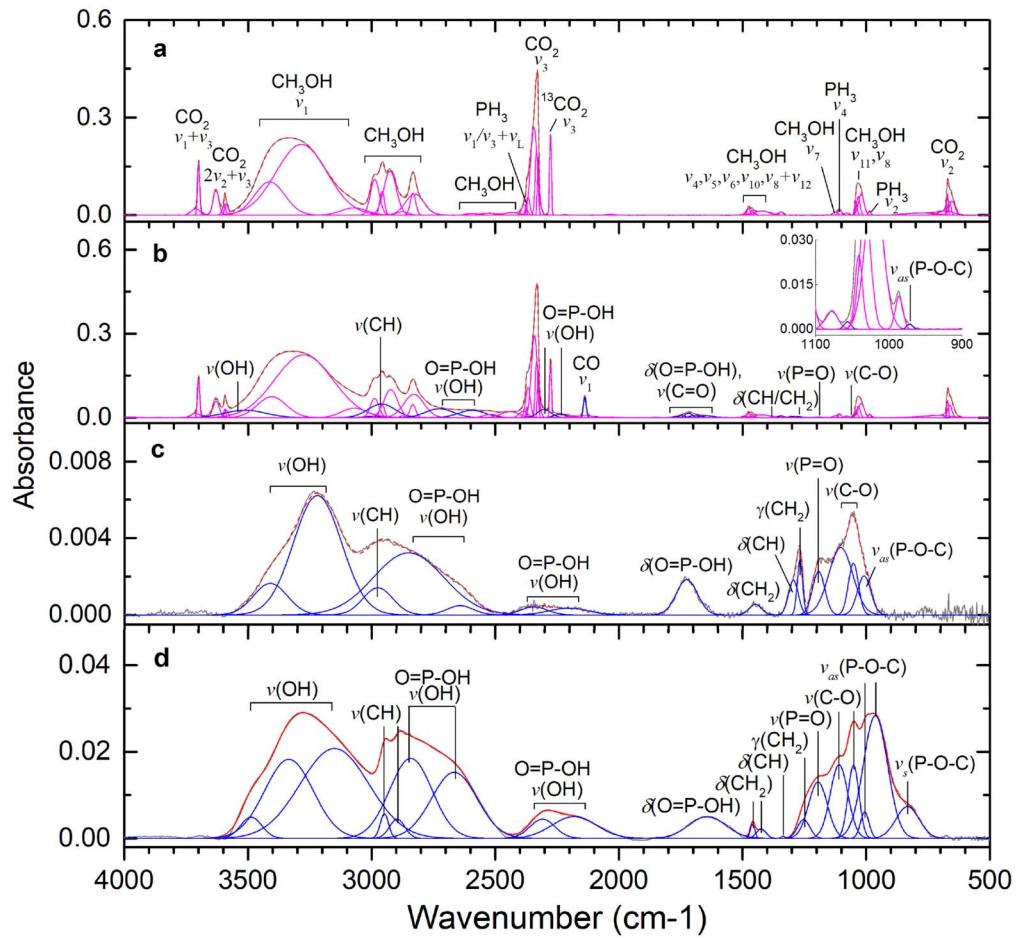


Figure A1. Deconvoluted infrared spectra of $\text{PH}_3 + \text{CH}_3\text{OH} + \text{CO}_2$ ice. (a) Pristine ices at 10 K. (b) After the low dose irradiation. (c) Residue at 300 K. For clarity, only significant peaks are labeled; detailed assignments can be found in Tables A3–A5. Panel (d) shows deconvoluted infrared spectrum of glycerol 1/3-phosphate.

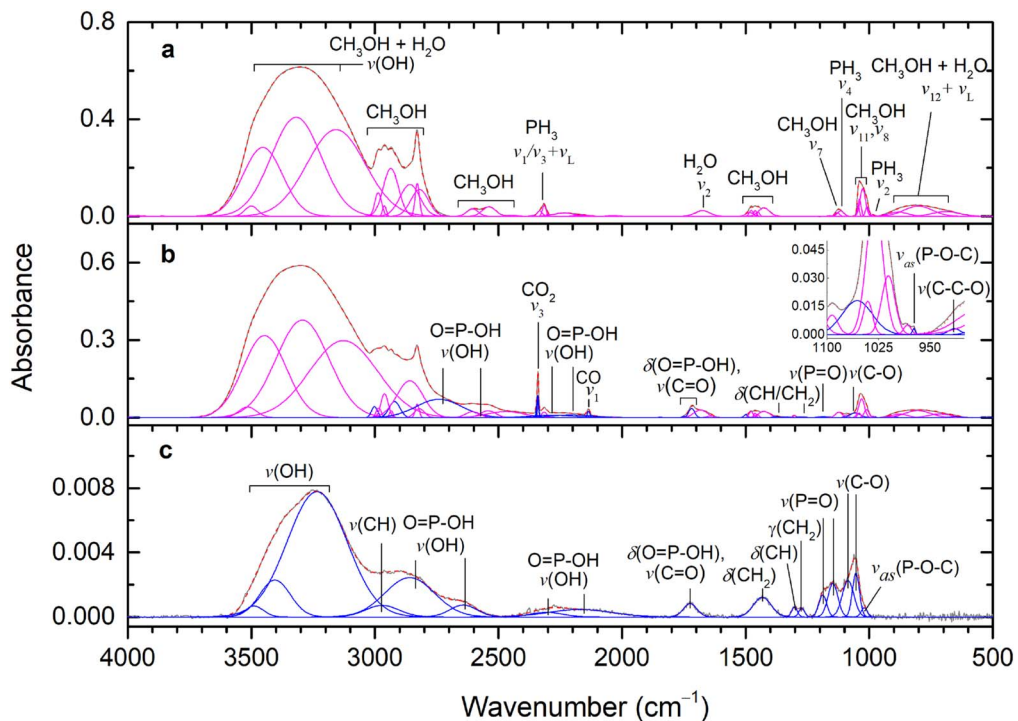


Figure A2. Deconvoluted infrared spectra of $\text{PH}_3 + \text{CH}_3\text{OH} + \text{H}_2\text{O}$ ice. (a) Pristine ices at 10 K. (b) After the low dose irradiation. (c) Residue at 300 K. For clarity, only significant peaks are labeled; detailed assignments can be found in Tables A6–A8.

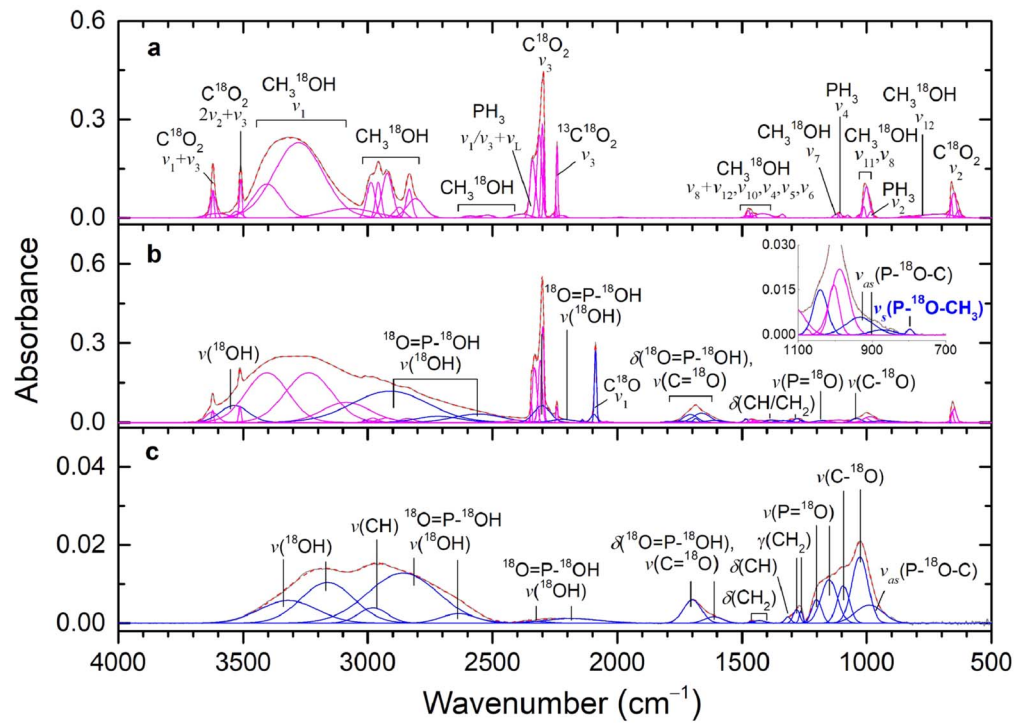


Figure A3. Deconvoluted infrared spectra of $\text{PH}_3 + \text{CH}_3^{18}\text{OH} + \text{C}^{18}\text{O}_2$ ice. (a) Pristine ices at 10 K. (b) After the high dose irradiation. (c) Residue at 300 K. For clarity, only significant peaks are labeled; detailed assignments can be found in Tables A9–A11.

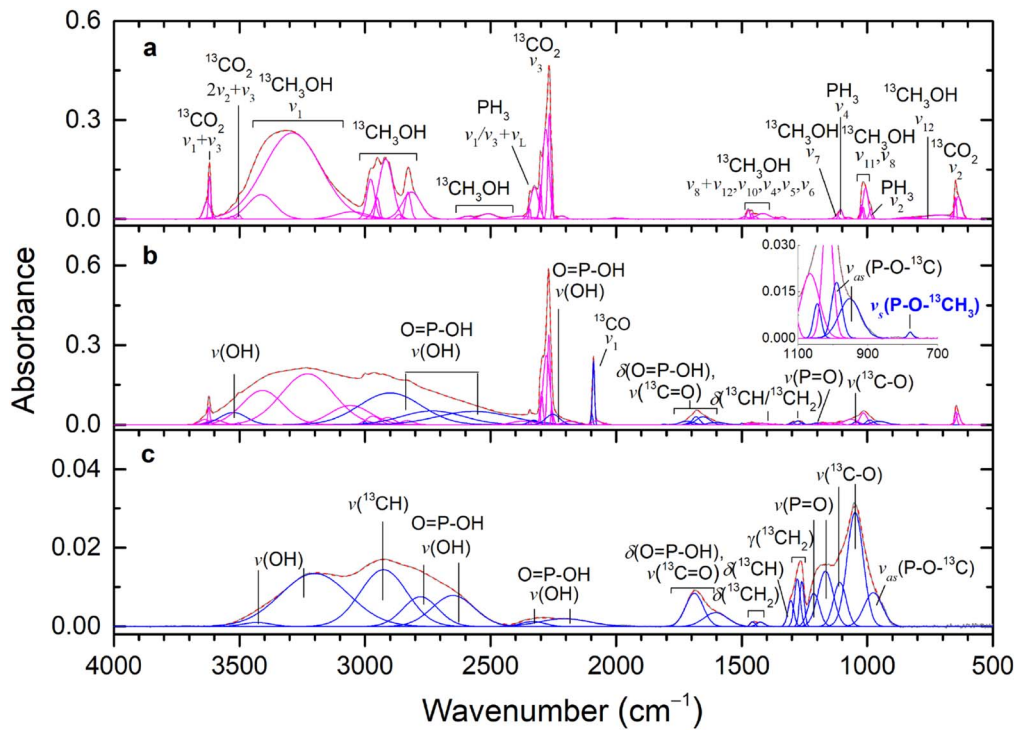


Figure A4. Deconvoluted infrared spectra of $\text{PH}_3 + {}^{13}\text{CH}_3\text{OH} + {}^{13}\text{CO}_2$ ice. (a) Pristine ices at 10 K. (b) After the high dose irradiation. (c) Residue at 300 K. For clarity, only significant peaks are labeled; detailed assignments can be found in Tables A12–A14.

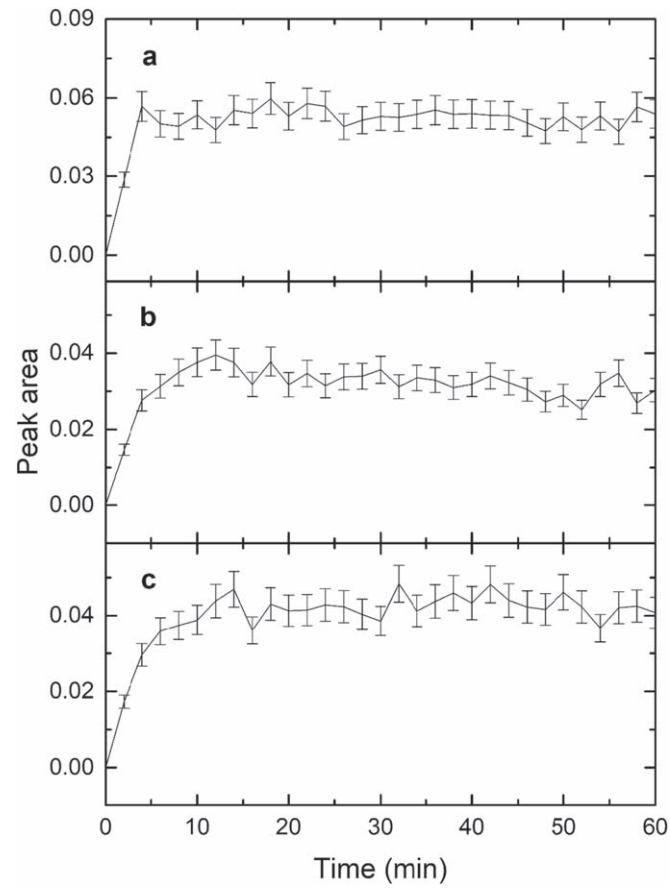


Figure A5. Temporal evolution of the symmetric P–O–C stretch band during the high dose irradiation. (a) $\text{PH}_3 + \text{CH}_3\text{OH} + \text{CO}_2$ (805 cm^{-1}). (b) $\text{PH}_3 + \text{CH}_3^{18}\text{OH} + \text{C}^{18}\text{O}_2$ (795 cm^{-1}). (c) $\text{PH}_3 + ^{13}\text{CH}_3\text{OH} + ^{13}\text{CO}_2$ (779 cm^{-1}).

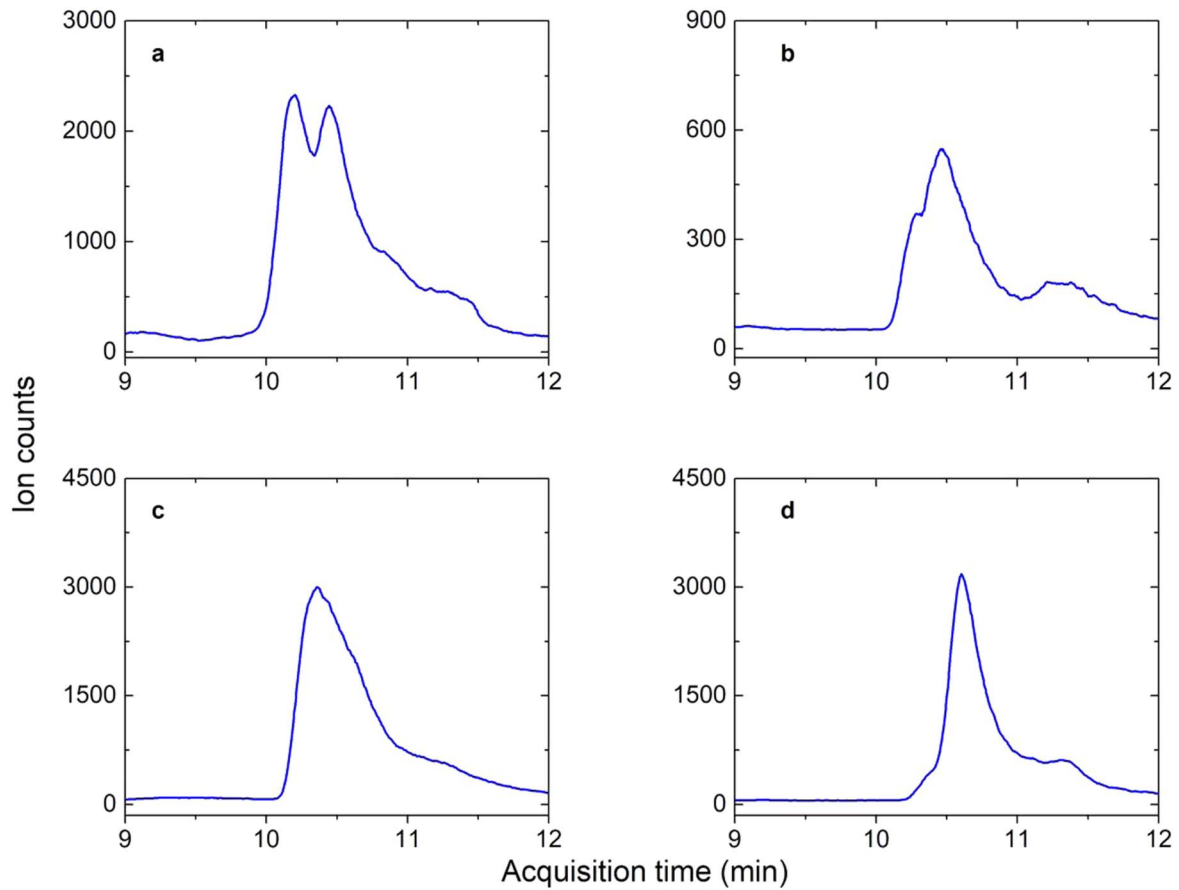


Figure A6. Chromatograms of the $m/z = 63$ fragment ions from $m/z = 171$, exploiting HPLC-QqQ-MS detection. (a) Residue of irradiated phosphine + methanol + water ice. (b) Calibration mixture of glycerol 2-phosphate (0.5 ng) and glycerol 1-/3-phosphate (0.5 ng). (c) Calibration sample of glycerol 2-phosphate (10 ng). (d) Calibration sample of glycerol 1-/3-phosphate (10 ng).

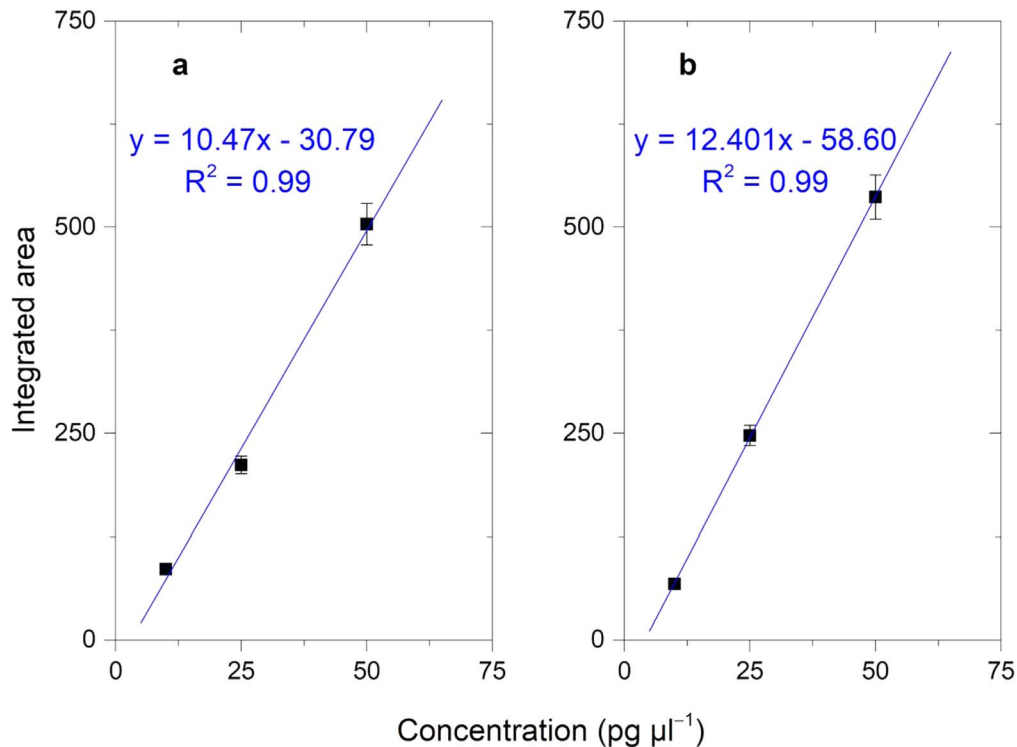


Figure A7. Correlation of concentration and integrated area of the quantifier $m/z = 171 \rightarrow m/z = 79$ transition: (a) glycerol 1/3-phosphate and (b) glycerol 2-phosphate.

Name	Structure	Cartesian coordinate (Å)				Vibrational frequency (cm ⁻¹) with IR intensities in parenthesis (km mol ⁻¹)		Relative energy (kJ mol ⁻¹)
		Atom	X	Y	Z			
Glycerol 1/3- phosphates		C	3.02117	0.78626	0.17414	24.0971 (-0.7259)	1046.0486 (73.828)	0
		C	1.8768	-0.14133	-0.21668	37.1262 (5.4847)	1066.6975 (205.7059)	
		C	0.56798	0.34299	0.368	83.2810 (4.7957)	1077.0488 (22.9593)	
		H	4.97967	0.64416	0.00347	95.645 (4.8673)	1092.9307 (135.8135)	
		H	3.00704	-1.70183	-0.02484	140.0782 (4.8167)	1145.6328 (33.6418)	
		H	-3.05443	-0.39919	-1.86557	184.5167 (59.6955)	1224.4073 (26.8438)	
		H	-3.05963	0.03281	1.82058	207.911 (7.6476)	1247.7683 (30.6794)	
		H	0.53571	0.12275	1.43603	225.0174 (70.5629)	1271.2654 (9.0127)	
		H	0.45035	1.41593	0.20867	234.9059 (31.8215)	1288.3518 (278.5048)	
		H	1.79137	-0.14063	-1.31015	252.1424 (49.5196)	1308.6784 (6.0165)	
		H	3.09295	0.84819	1.26481	315.7527 (2.3551)	1356.7697 (52.2957)	
		H	2.84831	1.78822	-0.23112	366.2852 (33.9262)	1400.171 (1.0042)	
		H	0.45035	1.41593	0.20867	383.235 (96.6504)	1438.1062 (0.135)	
		O	4.20891	0.21543	-0.37684	409.8786 (50.2753)	1459.4905 (3.4462)	

Figure A8. Computed Cartesian coordinates, vibrational frequencies, IR intensities, and relative energies for glycerol 1/3- and 2-phosphates.

		O	2.11667	-1.45773	0.25335	570.4321 (12.6765)	3036.7207 (40.1004)	
						808.304 (12.7708)	3040.3179 (26.0112)	
		O	-0.5166	-0.34919	-0.28599	883.346 (116.1523)	3091.5572 (14.8159)	
		O	-2.28655	1.57439	-0.22971	900.6357 (137.8975)	3785.3021 (57.6804)	
		O	-2.81853	-0.84108	-1.04207	919.9114 (288.237)	3818.0265 (143.0882)	
						934.628 (27.563)	3821.7685 (53.3277)	
		O	-2.35218	-0.46024	1.38971	1019.7411 (213.8608)	3838.0256 (53.3277)	
						1039.8162 (60.4362)		
		P	-2.01339	0.13397	-0.06149			
Glycerol 2- phosphates		C	-2.36044	-0.83919	-0.22946	41.2994 (0.7013)	1051.782 (58.8816)	4.7
						48.918 (3.5541)	1063.8935 (107.5179)	
		C	-1.30266	0.17419	0.1574	106.995 (18.2675)	1091.2222 (82.3252)	
		C	-1.71417	1.59858	-0.19406	117.1571 (9.8337)	1103.8351 (152.3906)	
		H	-2.59625	-2.77583	-0.04556	136.1426 (1.433)	1108.341 (12.0494)	
		H	2.0259	-2.1517	-0.66565	157.0051 (65.9366)	1225.4371 (28.5461)	
		H	2.0259	-2.1517	-0.66565	187.4979 (8.2268)	1242.3726 (15.8448)	
		H	2.69913	1.41203	0.30276	216.2888 (67.4229)	1277.6106 (4.0819)	
		H	2.69913	1.41203	0.30276	264.066 (35.7385)	1300.1075 (230.9325)	
		H	0.06841	2.40548	-0.21648	269.4877 (43.5376)	1313.3015 (30.8108)	
		H	-1.89364	1.66796	-1.2733	338.362 (30.0351)	1389.6643 (9.0626)	
		H	-1.89364	1.66796	-1.2733	365.4787 (22.3597)	1405.4805 (6.2636)	
		H	-2.64581	1.83597	0.32038	389.6421 (47.9988)	1428.2688 (26.1827)	
		H	-1.0838	0.09212	1.22266	413.7795 (130.3445)	1458.896 (0.2342)	
		H	-1.0838	0.09212	1.22266	417.7779 (17.7132)	1493.1177 (3.059)	
		H	-2.46976	-0.84895	-1.31891	450.1252 (10.4013)	1506.7948 (3.7198)	
		H	-3.31336	-0.52841	0.2132	479.1137 (66.3343)	2987.3129 (13.4343)	
		O	-1.96695	-2.11544	0.25645	515.9476 (35.8695)	2995.059 (75.544)	
		O	-1.96695	-2.11544	0.25645	559.9914 (30.0855)	3024.1871 (24.2868)	
		O	-0.0939	-0.14691	-0.58612	740.7497 (16.9688)	3071.3214 (2.6361)	
O	1.39854	-0.60946	1.51876	852.9497 (99.6764)	3083.6823 (31.8026)			
O	1.39854	-0.60946	1.51876	908.7282 (277.5263)	3771.0005 (102.2761)			
O	2.12493	-1.22477	-0.91323	912.0502 (11.4071)	3810.3732 (156.3147)			
O	1.98067	1.17257	-0.2945	996.119 (259.913)	3812.6219 (92.3585)			
O	-0.77178	2.56475	0.22969	1028.5611 (102.0755)	3829.9832 (42.1352)			
P	1.34004	-0.25574	0.09127	1049.2585 (93.9122)				

Figure A8. (Continued.)

ORCID iDs

Cheng Zhu  <https://orcid.org/0000-0002-7256-672X>
 Ralf I. Kaiser  <https://orcid.org/0000-0002-7233-7206>
 Gary Siuzdak  <https://orcid.org/0000-0002-4749-0014>
 Ryan C. Fortenberry  <https://orcid.org/0000-0003-4716-8225>

References

- Agúndez, M., Cernicharo, J., Decin, L., Encrenaz, P., & Teyssier, D. 2014, *ApJL*, **790**, L27
- Altwegg, K., Balsiger, H., Bar-Nun, A., et al. 2016, *SciA*, **2**, e1600285
- Arumainayagam, C. R., Garrod, R. T., Boyer, M. C., et al. 2019, *CSR*, **48**, 2293
- Balucani, N. 2009, *IJMS*, **10**, 2304
- Bangham, A. D. 1968, *PrBMB*, **18**, 29
- Becke, A. D. 1993, *JChPh*, **98**, 5648
- Bottinelli, S., Boogert, A. C. A., Bouwman, J., et al. 2010, *ApJ*, **718**, 1100
- Boyer, M. C., Rivas, N., Tran, A. A., Verish, C. A., & Arumainayagam, C. R. 2016, *SurSc*, **652**, 26
- Bunton, C. A., & Farber, S. J. 1969, *JInCh*, **34**, 3396
- Cherchneff, I. 2011, *A&A*, **526**, L11
- Cooper, G. W., Onwo, W. M., & Cronin, J. R. 1992, *GeCoA*, **56**, 4109
- Dartois, E., Schutte, W. A., Geballe, T. R., et al. 1999, *A&A*, **342**, L32
- Dohnalek, Z., Kimmel, G. A., Ayotte, P., Smith, R. S., & Kay, B. D. 2003, *JChPh*, **118**, 364
- Drouin, D., Couture, A. R., Joly, D., et al. 2007, *Scanning*, **29**, 92
- Fernández-García, C., Coggins, A. J., & Powner, M. W. 2017, *Life*, **7**, 31
- Frisch, M., Trucks, G., Schlegel, H., et al. 2009, Gaussian 09, Revision D. 01 (Wallingford, CT, USA: Gaussian)
- Gibard, C., Bhowmik, S., Karki, M., Kim, E.-K., & Krishnamurthy, R. 2018, *NatCh*, **10**, 212
- Gull, M., Zhou, M., Fernández, F. M., & Pasek, M. A. 2014, *JMolE*, **78**, 109
- Hudson, R. L., Loeffler, M. J., Ferrante, R. F., Gerakines, P. A., & Coleman, F. M. 2020, *ApJ*, **891**, 22
- Huh, S. B., & Lee, J. S. 2003, *JChPh*, **118**, 3035
- Jiménez-Serra, I., Viti, S., Quénard, D., & Holdship, J. 2018, *ApJ*, **862**, 128
- Kaiser, R. I., Maity, S., & Jones, B. M. 2015, *ACHIE*, **54**, 195
- Kaiser, R. I., Stockton, A. M., Kim, Y. S., Jensen, E. C., & Mathies, R. A. 2013, *ApJ*, **765**, 111
- Larson, H. P., Fink, U., Smith, H. A., & Davis, D. S. 1980, *ApJ*, **240**, 327
- Lodish, H., Berk, A., Zipursky, S. L., et al. 2000, *Molecular Cell Biology* (4th ed.; New York: W. H. Freeman)
- Loeffler, M. J., Moore, M. H., & Gerakines, P. A. 2016, *ApJ*, **827**, 98
- Loeffler, M. J., Raut, U., Vidal, R. A., Baragiola, R. A., & Carlson, R. W. 2006, *Icar*, **180**, 265
- Luna, R., Molpeceres, G., Ortigoso, J., et al. 2018, *A&A*, **617**, A116
- Nam, I., Lee, J. K., Nam, H. G., & Zare, R. N. 2017, *PNAS*, **114**, 12396
- Nuevo, M., Cooper, G., & Sandford, S. A. 2018, *NatCo*, **9**, 1
- Pasek, M. A., Harnmeijer, J. P., Buick, R., Gull, M., & Atlas, Z. 2013, *PNAS*, **110**, 10089
- Peterson, K. A., & Dunning Jr., T. H. 1995, *JChPh*, **102**, 2032
- Pontoppidan, K. M., Boogert, A. C. A., Fraser, H. J., et al. 2008, *ApJ*, **678**, 1005
- Raghavachari, K., Trucks, G. W., Pople, J. A., & Head-Gordon, M. 1989, *CPL*, **157**, 479
- Ridgway, S. T., Wallace, L., & Smith, G. R. 1976, *ApJ*, **207**, 1002
- Satorre, M. A., Domingo, M., Millán, C., et al. 2008, *P&SS*, **56**, 1748
- Schwartz, A. W. 2006, *RSPTB*, **361**, 1743
- Socrates, G. 2004, *Infrared and Raman Characteristic Group Frequencies* (3rd ed.; New York: Wiley)
- Teolis, B. D., Loeffler, M. J., Raut, U., Famá, M., & Baragiola, R. A. 2007, *Icar*, **190**, 274
- Turner, A. M., Abplanalp, M. J., Chen, S. Y., et al. 2015, *PCCP*, **17**, 27281
- Turner, A. M., Bergantini, A., Abplanalp, M. J., et al. 2018, *NatCo*, **9**, 3851
- Walde, P. 2006, *OLEB*, **36**, 109
- Weidenschilling, S. J. 2000, *SSRv*, **92**, 295
- Werner, H. J., Knowles, P. J., Knizia, G., et al. 2015, MOLPRO, Version 2015.1, a Package of ab Initio Programs, see <http://www.molpro.net>
- Wishart, D. S., Feunang, Y. D., Marcu, A., et al. 2018, *Nucleic Acids Research*, **46**, D608
- Yeghikyan, A. G. 2011, *Ap*, **54**, 87
- Yeghikyan, A. G., & Barsamyan, L. 2013, *Ap*, **56**, 443
- Yu, T., & Peng, H. 2010, *BMC bioinformatics*, **11**, 559
- Zhu, C., Frigge, R., Bergantini, A., Fortenberry, R. C., & Kaiser, R. I. 2019, *ApJ*, **881**, 156
- Zhu, C., Turner, A. M., Abplanalp, M. J., & Kaiser, R. I. 2018, *ApJS*, **234**, 15